

# The alignment of interstellar dust grains: thermal flipping and the Davis-Greenstein mechanism

Joseph C. Weingartner<sup>1</sup>★, Erald Kolasi<sup>1</sup>, and Cameron Woods<sup>1</sup>

<sup>1</sup>*Department of Physics and Astronomy, George Mason University, 4400 University Drive, Fairfax, VA 22030, USA*

Accepted XXX. Received YYY; in original form ZZZ

## ABSTRACT

Interstellar dust grains are non-spherical and, in some environments, partially aligned along the direction of the interstellar magnetic field. Numerous alignment theories have been proposed, all of which examine the grain rotational dynamics. In 1999, Lazarian & Draine introduced the important concept of thermal flipping, in which internal relaxation processes induce the grain body to flip while its angular momentum remains fixed. Through detailed numerical simulations, we study the role of thermal flipping on the grain dynamics during periods of relatively slow rotation, known as ‘crossovers’, for the special case of a spheroidal grain with a non-uniform mass distribution. Lazarian & Draine proposed that rapid flipping during a crossover would lead to ‘thermal trapping’, in which a systematic torque, fixed relative to the grain body, would time average to zero, delaying spin-up to larger rotational speeds. We find that the time-averaged systematic torque is not zero during the crossover and that thermal trapping is not prevalent. As an application, we examine whether the classic Davis-Greenstein alignment mechanism is viable, for grains residing in the cold neutral medium and lacking superparamagnetic inclusions. We find that Davis-Greenstein alignment is not hindered by thermal trapping, but argue that it is, nevertheless, too inefficient to yield the alignment of large grains responsible for optical and infrared starlight polarization. Davis-Greenstein alignment of small grains could potentially contribute to the observed ultraviolet polarization. The theoretical and computational tools developed here can also be applied to analyses of alignment via radiative torques and rotational disruption of grains.

**Key words:** dust, extinction – ISM: magnetic fields

## 1 INTRODUCTION

In the classic Davis-Greenstein (‘D-G’) theory (Davis & Greenstein 1951), paramagnetic dissipation in rotating grains drives the grains into alignment with the interstellar magnetic field. However, disalignment due to random collisions with gas-phase particles renders this mechanism ineffective if the grain rotation is excited by those same collisions.

Purcell (1979) noted that grains are subject to systematic torques, fixed relative to the grain body, that can potentially drive them to suprathermal rotation. That is, the grain’s angular speed could exceed, by a factor of several or more, the thermal rotation rate  $\omega_T$  that results when random collisions with gas particles excite the rotation. Suprathermally rotating grains can avoid being disaligned by these same random collisions.

Purcell (1979) also noted that internal mechanisms can dissipate rotational kinetic energy into heat within the grain, driving it to rotate around its principal axis of greatest moment of inertia, henceforth denoted  $\hat{a}_1$ . Purcell (1979) described a previously unexamined

mechanism, ‘Barnett dissipation’, in which a paramagnetic grain attempts to magnetize along the direction of the Barnett-equivalent field  $\mathbf{B}_{BE} = \boldsymbol{\omega}/\gamma_g$ . Here  $\boldsymbol{\omega}$  is the grain’s angular velocity vector, which rapidly varies as observed in a reference frame fixed to the grain when the grain does not rotate about a principal axis, and  $\gamma_g$  is the gyromagnetic ratio of the microscopic spins that give rise to the grain’s paramagnetism. Purcell (1979) considered dissipation associated with electron paramagnetism. Lazarian & Draine (1999b) described the related phenomenon of ‘nuclear relaxation’, associated with nuclei such as H that are likely incorporated within grains, and found that it can be much more efficient than Barnett dissipation for thermally rotating grains of a wide range of sizes.

The dominant systematic torque considered by Purcell (1979) is due to the recoil from H<sub>2</sub> molecules that form on the grain surface and are subsequently ejected into the gas, with some of the released binding energy converted to translational kinetic energy. If the molecules form only at certain special sites on the surface, then the net recoil torque is non-zero. In this work, we neglect gas-grain drift and photodesorption of adatoms; with these assumptions, the net recoil torque is fixed relative to the grain body. The special sites are not permanent; new sites form and old sites disappear as

★ E-mail: jweinga1@gmu.edu

the grain undergoes resurfacing, e.g. due to the accretion of atoms from the gas. As a result, the component  $\Gamma_1$  of the mean systematic torque along  $\hat{\mathbf{a}}_1$  can sometimes change sign. For a suprathermally rotating grain, in which Barnett dissipation is highly efficient,  $\omega$  is either nearly parallel to or nearly anti-parallel to  $\hat{\mathbf{a}}_1$ . Thus, when  $\Gamma_1$  changes sign, the grain enters a period of spin-down, and may ultimately spend some time rotating thermally. During these episodes, known as ‘crossovers’, the grain is again susceptible to disalignment via random collisions with gas particles. In the first study of crossovers, Spitzer & McGlynn (1979) concluded that a grain would become disaligned after passing through a small number of crossovers.

In the inverse process of Barnett dissipation, thermal fluctuations prevent  $\omega$  from lying exactly along  $\hat{\mathbf{a}}_1$  during periods of suprathermal rotation. Surprisingly, Lazarian & Draine (1997) found that this limits the extent of disalignment during crossovers. However, Lazarian & Draine (1999a) concluded that Barnett fluctuations are so strong during periods of thermal rotation that a grain can flip. That is, the sign of  $\mathbf{J} \cdot \hat{\mathbf{a}}_1$  can change as a result of thermal fluctuations;  $\mathbf{J}$  is the grain’s angular momentum. Lazarian & Draine (1999a) called this process ‘thermal flipping’.

When the grain flips, so does the direction of the systematic torque relative to the angular momentum vector  $\mathbf{J}$ . Denoting the interval between consecutive flips as an ‘f-step’, the time-averaged systematic torque will equal zero if the mean f-step duration is the same for the case that  $\mathbf{J} \cdot \hat{\mathbf{a}}_1 < 0$  as for the case that  $\mathbf{J} \cdot \hat{\mathbf{a}}_1 > 0$ . (In making this statement, we neglect any grain resurfacing during a crossover, as well as the dependence of the systematic torque on the grain kinetic energy at fixed angular momentum, and assume that the f-step duration is much less than the crossover duration.) As a result, the time required for the grain to emerge from a crossover may be much longer than for the case where thermal flipping does not occur and the effect of the systematic torque compounds uniformly over time. Lazarian & Draine (1999a) called this phenomenon ‘thermal trapping’. Analyzing nuclear relaxation, Lazarian & Draine (1999b) concluded that all grains that contribute to starlight polarization would likely undergo thermal trapping, arguing against Davis-Greenstein alignment aided by suprathermal spin-up due to torques fixed relative to the grain body.

For simplicity, the above studies focused on oblate grains exhibiting dynamic symmetry. That is,  $I_1 > I_2 = I_3$ , where  $I_i$  is the moment of inertia associated with principal axis  $\hat{\mathbf{a}}_i$ . Weingartner (2009) showed that thermal flipping does not actually occur for grains with dynamic symmetry. Weingartner (2009) noted that external processes (e.g. collisions with gas atoms and the ejection of  $\text{H}_2$  molecules from the grain surface) might induce grain flipping; Hoang & Lazarian (2009) examined this possibility quantitatively.

Kolasi & Weingartner (2017) showed that thermal flipping does occur for grains that lack dynamic symmetry. They only provided quantitative results for the relaxation rate for Barnett relaxation. In Section 2 of this work, we extend their analysis to also treat nuclear relaxation.

Furthermore, we challenge the assumption noted above, that the mean f-step duration is the same for the case that  $\mathbf{J} \cdot \hat{\mathbf{a}}_1 < 0$  as for the case that  $\mathbf{J} \cdot \hat{\mathbf{a}}_1 > 0$ . Because of the systematic torque, the magnitude  $J$  of the angular momentum is more likely to increase when  $\mathbf{J} \cdot \Gamma_1 \hat{\mathbf{a}}_1 > 0$  and is more likely to decrease when  $\mathbf{J} \cdot \Gamma_1 \hat{\mathbf{a}}_1 < 0$ . We will refer to an f-step with  $\mathbf{J} \cdot \Gamma_1 \hat{\mathbf{a}}_1 > 0$  as an ‘up-step’ and an f-step with  $\mathbf{J} \cdot \Gamma_1 \hat{\mathbf{a}}_1 < 0$  as a ‘down-step’. (Note that  $J$  can decrease during an up-step or increase during a down-step since gas-atom collisions and  $\text{H}_2$ -formation events occur stochastically.) In addition, the flipping probability per unit time decreases as  $J$

increases. Thus, the mean f-step duration is longer for f-steps in which  $J$  increases than for f-steps in which  $J$  decreases. We conclude that the mean duration is longer for up-steps than for down-steps. In other words, there is a bias for f-steps to have longer duration when the systematic torque acts to spin the grain up than when it acts to spin the grain down. Consequently, the systematic torque does not average to zero, potentially circumventing thermal trapping. The main purpose of this work is to examine this possibility, employing detailed numerical simulations.

For simplicity, we consider an oblate spheroidal grain with an inhomogeneous mass distribution. Thus, the grain exhibits geometric symmetry but not dynamic symmetry. We assume that the mass is distributed such that the grain’s center of mass remains at its geometric center and the principal axis of largest moment of inertia,  $\hat{\mathbf{a}}_1$ , lies along the symmetry axis, but  $I_2 \neq I_3$ .

The equations and quantities used in the simulations are derived in Sections 3–6. Section 7 describes the fundamental elements of the simulations. Section 8 presents a test of the simulation code. Two simplified versions of the code are used to examine the case where the grain is in thermal equilibrium, for which analytic results are available for comparison. The codes successfully reproduce the expected results. Section 9 describes our treatment of  $\text{H}_2$  formation (and subsequent ejection) at special surface sites. Sections 10–12 contain our main simulation results, focusing on grain dynamics in the cold neutral medium of the diffuse ISM. Section 10 presents simulation results for one specific case, demonstrating that the mean up-step duration exceeds the mean down-step duration in that case. Section 11 presents results from large suites of simulations examining crossovers, specifically their duration and the associated grain disorientation. We find that thermal trapping is not prevalent. The simulations in Section 12 examine the efficiency of Davis-Greenstein alignment in the cold neutral medium. We find that thermal trapping does not inhibit suprathermal spin-up and D-G alignment, but the alignment time-scale (for grains lacking superparamagnetic inclusions) is uncomfortably long. Conclusions and future work are summarized in Section 13.

## 2 NUCLEAR RELAXATION IN NON-SYMMETRIC GRAINS

Consider a non-symmetric grain with  $I_1 > I_2 > I_3$  and denote  $r_2 = I_1/I_2$  and  $r_3 = I_1/I_3$ . It is convenient to define a dimensionless measure of the grain’s rotational kinetic energy  $E$  (when  $J$  is constant),

$$q = \frac{2I_1 E}{J^2}. \quad (1)$$

The kinetic energy is minimized (maximized) for rotation about  $\hat{\mathbf{a}}_1$  ( $\hat{\mathbf{a}}_3$ ); thus,  $1 \leq q \leq r_3$ . In the absence of external processes, the evolution of  $q$  due to internal relaxation can be described using the Langevin equation,

$$dq = A(q) dt + \sqrt{D(q)} dw_{\text{int}}, \quad (2)$$

where  $dt$  is a time step,  $dw_{\text{int}}$  is a Gaussian random variable with variance  $dt$ , the drift coefficient  $A(q)$  is proportional to the average energy dissipation rate, and  $D(q)$  is the diffusion coefficient.

Kolasi & Weingartner (2017) examined Barnett relaxation in non-symmetric grains, deriving expressions for the drift and diffusion coefficients in the low-frequency limit, i.e. when the angular frequency of the grain’s rotation is much less than  $T_2^{-1}$ , where  $T_2$  is the spin-spin relaxation time. For Barnett relaxation, associated

with electrons in, e.g., Fe atoms, this approximation is excellent. However, in the case of nuclear relaxation, it can fail for thermally rotating grains. Nuclear relaxation dominates Barnett relaxation for most thermally rotating grains. Thus, in this section, we relax the low-frequency limit. Readers who are not familiar with [Kolasi & Weingartner \(2017\)](#) may want to proceed directly to the results in the final two paragraphs of this section.

The only term in the [Kolasi & Weingartner \(2017\)](#) expression for the drift coefficient  $A(q)$  that changes when the low-frequency limit is relaxed is the following function, which is equivalent to the expression on the second line in their equation (49):

$$\Theta(q, \Psi) = (T_2')^{-2} \int_0^{4K(k^{\pm 2})} du \left\{ c_1(q) \mathcal{F}_{\pm}(u, k^{\pm 2}) \times \left[ c_1(q) \mathcal{F}_{\pm}(u, k^{\pm 2}) - M_1'(q, u) \right] + c_2(q) \text{sn}(u, k^{\pm 2}) \times \left[ c_2(q) \text{sn}(u, k^{\pm 2}) - M_2'(q, u) \right] + c_3(q) \mathcal{F}_{\mp}(u, k^{\pm 2}) \times \left[ c_3(q) \mathcal{F}_{\mp}(u, k^{\pm 2}) - M_3'(q, u) \right] \right\} \quad (3)$$

where the  $+$  ( $-$ ) sign in  $k^{\pm 2}$  and  $\mathcal{F}_{\pm}$  is for  $1 < q < r_2$  ( $r_2 < q < r_3$ );

$$T_2' = \Psi \times \begin{cases} [(r_2 - 1)(r_3 - q)]^{1/2} & 1 < q < r_2 \\ [(r_3 - r_2)(q - 1)]^{1/2} & r_2 < q < r_3 \end{cases}; \quad (4)$$

$$\Psi = \frac{JT_2}{I_1}; \quad (5)$$

$K(k^{\pm 2})$  is the complete elliptic integral of the first kind,

$$k^2 = \frac{(r_3 - r_2)(q - 1)}{(r_2 - 1)(r_3 - q)}; \quad (6)$$

$\mathcal{F}_{+}(u, k^{\pm 2}) = \text{dn}(u, k^{\pm 2})$ ;  $\mathcal{F}_{-}(u, k^{\pm 2}) = \text{cn}(u, k^{\pm 2})$ ;  $\text{sn}(u, k^{\pm 2})$ ,  $\text{cn}(u, k^{\pm 2})$ , and  $\text{dn}(u, k^{\pm 2})$ , are the Jacobi elliptic functions;

$$c_1(q) = \begin{cases} [(r_2 - 1)(r_3 - 1)]^{-1/2} & , 1 < q < r_2 \\ (r_3 - q)^{1/2} [(r_3 - 1)(r_3 - r_2)(q - 1)]^{-1/2} & , r_2 < q < r_3 \end{cases}; \quad (7)$$

$$c_2(q) = \begin{cases} -r_2(q - 1)^{1/2}(r_2 - 1)^{-1}(r_3 - q)^{-1/2} & , 1 < q < r_2 \\ -r_2(r_3 - q)^{1/2}(r_3 - r_2)^{-1}(q - 1)^{-1/2} & , r_2 < q < r_3 \end{cases}; \quad (8)$$

$$c_3(q) = r_3 \left( \frac{q - 1}{r_3 - q} \right)^{1/2} c_1(q); \quad (9)$$

and  $M_i'(q, u)$  are the steady-state solutions of the following differential equations:

$$\frac{dM_1'}{du} = c_3(q)M_2'(q, u)\mathcal{F}_{\mp}(u, k^{\pm 2}) - c_2(q)M_3'(q, u)\text{sn}(u, k^{\pm 2}) + (T_2')^{-1} \left[ c_1(q)\mathcal{F}_{\pm}(u, k^{\pm 2}) - M_1'(u) \right], \quad (10)$$

$$\frac{dM_2'}{du} = c_1(q)M_3'(q, u)\mathcal{F}_{\pm}(u, k^{\pm 2}) - c_3(q)M_1'(q, u)\mathcal{F}_{\mp}(u, k^{\pm 2}) + (T_2')^{-1} \left[ c_2(q)\text{sn}(u, k^{\pm 2}) - M_2'(u) \right], \quad (11)$$

$$\frac{dM_3'}{du} = c_2(q)M_1'(q, u)\text{sn}(u, k^{\pm 2}) - c_1(q)M_2'(q, u)\mathcal{F}_{\pm}(u, k^{\pm 2}) + (T_2')^{-1} \left[ c_3(q)\mathcal{F}_{\mp}(u, k^{\pm 2}) - M_3'(u) \right]. \quad (12)$$

We adopt the same conventions for the Jacobi elliptic functions as [Weingartner & Draine \(2003\)](#).

From [Kolasi & Weingartner \(2017\)](#), in the low-frequency limit

$$\Theta(q, \Psi \ll 1) = \frac{4 \{ z_1 [E(k^2) + (k^2 - 1)K(k^2)] + k^2 z_2 E(k^2) \} (q - 1)}{3k^2(r_2 - 1)^2(r_3 - 1)(r_3 - q)} \quad (13)$$

when  $1 < q < r_2$  and

$$\Theta(q, \Psi \ll 1) = 4 \left\{ z_1 [E(k^{-2}) + (k^{-2} - 1)K(k^{-2})] + k^{-2} z_1 E(k^{-2}) \right\} \times \frac{(r_3 - q)}{3k^{-2}(r_3 - r_2)^2(r_3 - 1)(q - 1)} \quad (14)$$

when  $r_2 < q < r_3$ ;  $E(k^2)$  is the complete elliptic integral of the second kind,

$$z_1 = 2(r_3 - r_2) - r_2^2(r_2 - 1) + r_2^2(r_3 - 1), \quad (15)$$

and

$$z_2 = -(r_3 - r_2) + 2r_3^2(r_2 - 1) + r_2^2(r_3 - 1). \quad (16)$$

For the specific case that  $r_2 = 1.3$  and  $r_3 = 1.5$ , we find the steady-state solution of equations (10)–(12) and perform the integration in equation (3) numerically. We find that  $\Theta(q, \Psi)$  is very close to  $\Theta(q, \Psi \ll 1)$  when  $\Psi \lesssim 0.1$  and  $\Theta(q, \Psi)/\Theta(q, \Psi \ll 1)$  drops to  $\approx 6 \times 10^{-3}$  when  $\Psi = 10$ . For a given value of  $\Psi$ ,  $\Theta(q, \Psi)/\Theta(q, \Psi \ll 1)$  varies by less than 30 per cent as  $q$  ranges from 1 to  $r_3$ .

[Kolasi & Weingartner \(2017\)](#) expressed the drift coefficient  $A(q)$  in the low-frequency limit in the form  $A(q) = -\tau_{\text{int}}^{-1} A_1(q)$ , where  $A_1(q)$  is a dimensionless function of  $q$ , given in equations (55) and (61) in [Kolasi & Weingartner \(2017\)](#), and  $\tau_{\text{int}}$  is the internal relaxation time-scale. Given the gross uncertainties in the theoretical modeling of Barnett and nuclear relaxation, we do not adjust the functional form of  $A_1(q)$  from its low-frequency form. Rather, we simply adjust the relaxation time-scale according to

$$\tau_{\text{int}}(\Psi) = \tau_{\text{int}}(\Psi \ll 1) \left[ \frac{\Theta(q, \Psi \ll 1)}{\Theta(q, \Psi)} \right]_{\text{av}}. \quad (17)$$

In the final term in equation (17), the ratio  $\Theta(q, \Psi \ll 1)/\Theta(q, \Psi)$  is averaged over  $q$  for a fixed value of  $\Psi$ . To within 0.5 per cent,

$$\left[ \frac{\Theta(q, \Psi \ll 1)}{\Theta(q, \Psi)} \right]_{\text{av}} = \left( 1 + 1.67 \Psi^{1.96} \right)^{1.02}. \quad (18)$$

Note that this fit is specifically for grains with  $r_2 = 1.3$  and  $r_3 = 1.5$ .

From equation (56) in [Kolasi & Weingartner \(2017\)](#),

$$\tau_{\text{int}}(\Psi \ll 1) = \frac{\gamma_g^2 I_1^3}{2\chi_0 V T_2 J^2}. \quad (19)$$

As in [Weingartner & Draine \(2003\)](#), we take  $\gamma_g = -1.76 \times 10^7 \text{ s}^{-1} \text{ G}^{-1}$  and  $\chi_0 T_2 = 10^{-13} (15 \text{ K}/T_d) \text{ s}$  for Barnett relaxation ( $T_d$  is the dust temperature) and  $\gamma_g = 1.3 \times 10^4 \text{ s}^{-1} \text{ G}^{-1}$ ,  $\chi_0 = 4 \times 10^{-11} (15 \text{ K}/T_d)$ , and  $T_2 = 10^{-4} \text{ s}$  for nuclear relaxation. For Barnett relaxation, we assume that the low-frequency limit always applies.

### 3 SPHEROID PROPERTIES

Consider a spheroid characterized by the radius  $a_{\text{eff}}$  of a sphere with equal volume, the ratio  $\delta$  of the semilength  $a$  along the (geometric) symmetry axis to the semilength  $b$  along a perpendicular axis, and the average mass density  $\bar{\rho}$ . (Recall that we take the density to vary throughout the grain, so that dynamic symmetry is violated.) When  $\delta > 1$  the spheroid is prolate and when  $\delta < 1$  the spheroid is oblate. In either case,  $a = a_{\text{eff}} \delta^{2/3}$ . Denote the principal axes  $\hat{\mathbf{a}}_1$ ,  $\hat{\mathbf{a}}_2$ , and  $\hat{\mathbf{a}}_3$ , with corresponding moments of inertia

$$I_i = \frac{8}{15} \pi \bar{\rho} a_{\text{eff}}^5 \alpha_i, \quad (20)$$

and take the symmetry axis to lie along  $\hat{\mathbf{a}}_1$ . We take  $\alpha_1 = \delta^{-2/3}$ , its value for a uniform spheroid, and assign smaller, but unequal, values to both  $\alpha_2$  and  $\alpha_3$ . For a uniform spheroid, these would be given by  $\alpha_2 = \alpha_3 = (\alpha_1 + \alpha_1^{-2})/2$ . Here, we consider an oblate grain with  $\delta = 0.5$  and take  $r_2 = \alpha_1/\alpha_2 = 1.3$  and  $r_3 = \alpha_1/\alpha_3 = 1.5$ . (One simple, albeit unrealistic, mass distribution reproducing these values for  $\alpha_1$ ,  $r_2$ , and  $r_3$  consists of a uniform mass distribution throughout the spheroid plus three point particles located at the surface of the grain along the  $a_1$ -,  $a_2$ -, and  $a_3$ -axes, with mass fractions, i.e. the mass of the point mass divided by the entire mass of the grain, of 0.2229, 0.0538, and 0.0949, respectively.)

It will be convenient to also denote  $(\hat{\mathbf{a}}_2, \hat{\mathbf{a}}_3, \hat{\mathbf{a}}_1)$  by  $(\hat{\mathbf{x}}, \hat{\mathbf{y}}, \hat{\mathbf{z}})$ . In order to evaluate mean torques and diffusion coefficients associated with gas-atom collisions and  $\text{H}_2$  formation, it is most convenient to adopt oblate spheroidal coordinates  $(\eta, \phi')$ . The transformation to grain-body Cartesian coordinates is

$$x = a_{\text{eff}} \delta^{-1/3} \cos \eta \cos \phi', \quad (21)$$

$$y = a_{\text{eff}} \delta^{-1/3} \cos \eta \sin \phi', \quad (22)$$

$$z = a_{\text{eff}} \delta^{2/3} \sin \eta, \quad (23)$$

and  $-\pi/2 \leq \eta \leq \pi/2$ ,  $0 \leq \phi' < 2\pi$ . The surface area element is

$$dS = a_{\text{eff}}^2 \delta^{-2/3} \left[ \delta^2 + (1 - \delta^2) \sin^2 \eta \right]^{1/2} \cos \eta d\eta d\phi' \quad (24)$$

and the outward-pointing unit normal is

$$\hat{\mathbf{N}} = \left[ \delta^2 + (1 - \delta^2) \sin^2 \eta \right]^{-1/2} \times \left[ \delta \cos \eta (\hat{\mathbf{x}} \cos \phi' + \hat{\mathbf{y}} \sin \phi') + \hat{\mathbf{z}} \sin \eta \right]. \quad (25)$$

Along with  $\hat{\mathbf{N}}$ , the following two vectors form an orthonormal basis:

$$\hat{\phi}' = -\hat{\mathbf{x}} \sin \phi' + \hat{\mathbf{y}} \cos \phi', \quad (26)$$

$$\hat{\mathbf{t}} = \hat{\phi}' \times \hat{\mathbf{N}} = \left[ \delta^2 + (1 - \delta^2) \sin^2 \eta \right]^{-1/2} \times \left[ \sin \eta (\hat{\mathbf{x}} \cos \phi' + \hat{\mathbf{y}} \sin \phi') - \hat{\mathbf{z}} \delta \cos \eta \right]. \quad (27)$$

For later use, we define the following integrals over the coordinate  $\eta$ :

$$\mathcal{I}_1(\delta) = \int_{-\pi/2}^{\pi/2} d\eta \cos \eta [A(\delta, \eta)]^{-1} \sin^2 \eta = \frac{2 - \delta^2 - \delta^4 g(\delta)}{4(1 - \delta^2)}, \quad (28)$$

$$\mathcal{I}_2(\delta) = \int_{-\pi/2}^{\pi/2} d\eta \cos \eta [A(\delta, \eta)]^{-1} = 1 + \delta^2 g(\delta), \quad (29)$$

$$\mathcal{I}_3(\delta) = \int_{-\pi/2}^{\pi/2} d\eta \cos \eta A(\delta, \eta) = 2g(\delta), \quad (30)$$

$$\mathcal{I}_4(\delta) = \int_{-\pi/2}^{\pi/2} d\eta \cos \eta A(\delta, \eta) \sin^2 \eta \cos^2 \eta = \frac{2 + \delta^2 - \delta^2(4 - \delta^2)g(\delta)}{4(1 - \delta^2)^2}, \quad (31)$$

where

$$A(\delta, \eta) = \left[ \delta^2 + (1 - \delta^2) \sin^2 \eta \right]^{-1/2} \quad (32)$$

and

$$g(\delta) = \frac{1}{2} (1 - \delta^2)^{-1/2} \ln \left[ \frac{1 + (1 - \delta^2)^{-1/2}}{-1 + (1 - \delta^2)^{-1/2}} \right]. \quad (33)$$

### 4 COORDINATE SYSTEMS

We already introduced grain-body coordinates  $(x, y, z)$ , fixed with respect to the grain, in Section 3. Now consider an inertial coordinate system, which we call ‘alignment coordinates’  $(x_B, y_B, z_B)$ , with its origin also at the center of the spheroidal grain.

The orientation of the grain in space depends on its angular momentum  $\mathbf{J}$  and rotational kinetic energy  $E$ . We denote the spherical coordinates of  $\mathbf{J}$  in alignment coordinates by  $(J, \xi, \phi_B)$ . We define ‘angular-momentum coordinates’  $(x_J, y_J, z_J)$  by

$$\hat{\mathbf{x}}_J = \hat{\xi} = \hat{\mathbf{x}}_B \cos \xi \cos \phi_B + \hat{\mathbf{y}}_B \cos \xi \sin \phi_B - \hat{\mathbf{z}}_B \sin \xi, \quad (34)$$

$$\hat{\mathbf{y}}_J = \hat{\phi}_B = -\hat{\mathbf{x}}_B \sin \phi_B + \hat{\mathbf{y}}_B \cos \phi_B, \quad (35)$$

$$\hat{\mathbf{z}}_J = \hat{\mathbf{J}} = \hat{\mathbf{x}}_B \sin \xi \cos \phi_B + \hat{\mathbf{y}}_B \sin \xi \sin \phi_B + \hat{\mathbf{z}}_B \cos \xi. \quad (36)$$

The orientation of the grain body in angular-momentum coordinates can be expressed using Eulerian angles  $(\alpha, \gamma, \zeta)$ . We adopt the same prescription for the Eulerian angles as in section 2.5.3 in [Weingartner & Draine \(2003\)](#): Start with the grain axes  $(\hat{\mathbf{a}}_2, \hat{\mathbf{a}}_3, \hat{\mathbf{a}}_1)$  aligned with  $(\hat{\mathbf{x}}_J, \hat{\mathbf{y}}_J, \hat{\mathbf{z}}_J)$ . Then apply the following operations to the grain: (1) rotate through angle  $\zeta$  about  $\hat{\mathbf{a}}_1 = \hat{\mathbf{z}}_J$ , (2) rotate through angle  $\gamma$  about  $\hat{\mathbf{a}}_2$ , (3) rotate through angle  $\alpha$  about  $\hat{\mathbf{a}}_1$ . Thus, the transformation between grain-body and angular-momentum coordinates is

$$\hat{\mathbf{x}} = \hat{\mathbf{a}}_2 = \hat{\mathbf{x}}_J (\cos \alpha \cos \zeta - \sin \alpha \sin \zeta \cos \gamma) + \hat{\mathbf{y}}_J (\cos \alpha \sin \zeta + \sin \alpha \cos \zeta \cos \gamma) + \hat{\mathbf{z}}_J \sin \alpha \sin \gamma, \quad (37)$$

$$\hat{\mathbf{y}} = \hat{\mathbf{a}}_3 = -\hat{\mathbf{x}}_J (\sin \alpha \cos \zeta + \cos \alpha \sin \zeta \cos \gamma) + \hat{\mathbf{y}}_J (\cos \alpha \cos \zeta \cos \gamma - \sin \alpha \sin \zeta) + \hat{\mathbf{z}}_J \cos \alpha \sin \gamma, \quad (38)$$

$$\hat{\mathbf{z}} = \hat{\mathbf{a}}_1 = \hat{\mathbf{x}}_J \sin \zeta \sin \gamma - \hat{\mathbf{y}}_J \cos \zeta \sin \gamma + \hat{\mathbf{z}}_J \cos \gamma. \quad (39)$$

## 5 GRAIN ROTATION

A description of the free rotation of a non-symmetric grain, for a given  $J$  and  $q$ , and its flipping dynamics can be found in section 2.5 of Weingartner & Draine (2003). As described there, the components of the grain's angular velocity  $\omega$  along the principal axes involve the Jacobi elliptic functions. For later convenience, we reproduce the expressions for  $\omega_i$  from Kolasi & Weingartner (2017) here. When  $1 < q < r_2$ ,

$$\omega_1 = \pm \frac{J}{I_1} \left( \frac{r_3 - q}{r_3 - 1} \right)^{1/2} \text{dn}(\omega_{\text{rot}} t, k^2), \quad (40)$$

$$\omega_2 = -\frac{J}{I_1} r_2 \left( \frac{q - 1}{r_2 - 1} \right)^{1/2} \text{sn}(\omega_{\text{rot}} t, k^2), \quad (41)$$

$$\omega_3 = \pm \frac{J}{I_1} r_3 \left( \frac{q - 1}{r_3 - 1} \right)^{1/2} \text{cn}(\omega_{\text{rot}} t, k^2), \quad (42)$$

where

$$k^2 = \frac{(r_3 - r_2)(q - 1)}{(r_2 - 1)(r_3 - q)} \quad (43)$$

and

$$\omega_{\text{rot}} = \frac{J}{I_1} [(r_2 - 1)(r_3 - q)]^{1/2}. \quad (44)$$

The grain is in the positive flip state with respect to  $\hat{a}_1$  (i.e.  $\mathbf{J} \cdot \hat{a}_1 > 0$ ) when the plus sign is chosen in both equations (40) and (42). It is in the negative flip state with respect to  $\hat{a}_1$  when the minus sign is chosen in both of those cases. When  $r_2 < q < r_3$ ,

$$\omega_1 = \pm \frac{J}{I_1} \left( \frac{r_3 - q}{r_3 - 1} \right)^{1/2} \text{cn}(\omega_{\text{rot}} t, k^{-2}), \quad (45)$$

$$\omega_2 = -\frac{J}{I_1} r_2 \left( \frac{r_3 - q}{r_3 - r_2} \right)^{1/2} \text{sn}(\omega_{\text{rot}} t, k^{-2}), \quad (46)$$

$$\omega_3 = \pm \frac{J}{I_1} r_3 \left( \frac{q - 1}{r_3 - 1} \right)^{1/2} \text{dn}(\omega_{\text{rot}} t, k^{-2}), \quad (47)$$

with  $k^2$  as defined in equation (43) and

$$\omega_{\text{rot}} = \frac{J}{I_1} [(r_3 - r_2)(q - 1)]^{1/2}. \quad (48)$$

The grain is in the positive flip state with respect to  $\hat{a}_3$  (i.e.  $\mathbf{J} \cdot \hat{a}_3 > 0$ ) when the plus sign is chosen in both equations (45) and (47). It is in the negative flip state with respect to  $\hat{a}_3$  when the minus sign is chosen in both of those cases.

The components  $\omega_i$  can also be expressed in terms of the Eulerian angles:

$$\omega_1 = \frac{J}{I_1} \cos \gamma, \quad (49)$$

$$\omega_2 = \frac{J}{I_2} \sin \gamma \sin \alpha, \quad (50)$$

$$\omega_3 = \frac{J}{I_3} \sin \gamma \cos \alpha. \quad (51)$$

As seen in equations (40)–(42) and (45)–(47), the angular velocity in grain-body coordinates is periodic in variable  $\nu = \omega_{\text{rot}} t$ ,

with period  $4K(k^{\pm 2})$ , where the + (–) sign is for the case that  $1 < q < r_2$  ( $r_2 < q < r_3$ ). Thus, from equations (49)–(51), the Eulerian angles  $\alpha$  and  $\gamma$  are likewise periodic. The Eulerian angle  $\zeta$  can be expressed as the sum of two periodic functions, one with the same period as for  $\alpha$  and  $\gamma$  and the other with an incommensurate period. When evaluating drift and diffusion coefficients associated with external processes, we will average over the grain rotation, since the rotation time-scale is orders of magnitude smaller than all other relevant time-scales. Denoting the average of a function  $F$  over grain rotation by  $\langle F \rangle$ ,

$$\langle F \rangle = \left[ 8\pi K(k^{\pm 2}) \right]^{-1} \int_0^{4K(k^{\pm 2})} d\nu \int_0^{2\pi} d\zeta F[\alpha(\nu), \gamma(\nu), \zeta]. \quad (52)$$

For a grain with dynamic symmetry,  $\gamma$  is constant when  $J$  and  $E$  are fixed. As seen above,  $\gamma$  varies periodically for a grain that lacks dynamic symmetry. From equations (49), (40), and (45), the average value of  $\cos^2 \gamma$  is given by

$$\langle \cos^2 \gamma \rangle = \frac{r_3 - q}{r_3 - 1} \times \begin{cases} \langle \text{dn}^2(\nu, k^2) \rangle & , 1 < q < r_2 \\ \langle \text{cn}^2(\nu, k^{-2}) \rangle & , r_2 < q < r_3 \end{cases}. \quad (53)$$

The averages on the right-hand side of equation (53) can be expressed as

$$\langle \text{dn}^2(\nu, k^2) \rangle = \frac{E(k^2)}{K(k^2)} \quad (54)$$

and

$$\langle \text{cn}^2(\nu, k^2) \rangle = \frac{\langle \text{dn}^2(\nu, k^2) \rangle - 1 + k^2}{k^2}. \quad (55)$$

We will employ this result in Section 6, where we will also need the following results, all derived using equations (40)–(55):

$$\langle \sin^2 \gamma \sin^2 \alpha \rangle = \begin{cases} \left( 1 - \langle \text{dn}^2(\nu, k^2) \rangle \right) \frac{r_3 - q}{r_3 - r_2} & , 1 < q < r_2 \\ \left( 1 - \langle \text{dn}^2(\nu, k^{-2}) \rangle \right) \frac{q - 1}{r_2 - 1} & , r_2 < q < r_3 \end{cases}, \quad (56)$$

$$\langle \sin^2 \gamma \cos^2 \alpha \rangle = \frac{q - 1}{r_3 - 1} \times \begin{cases} \langle \text{cn}^2(\nu, k^2) \rangle & , 1 < q < r_2 \\ \langle \text{dn}^2(\nu, k^{-2}) \rangle & , r_2 < q < r_3 \end{cases}, \quad (57)$$

$$\langle \cos \gamma \rangle = \begin{cases} \pm \left( \frac{r_3 - q}{r_3 - 1} \right)^{1/2} \frac{\pi}{2K(k^2)} & , 1 < q < r_2 \\ 0 & , r_2 < q < r_3 \end{cases}, \quad (58)$$

$$\langle \sin \gamma \cos \alpha \rangle = \begin{cases} 0 & , 1 < q < r_2 \\ \pm \left( \frac{q - 1}{r_3 - 1} \right)^{1/2} \frac{\pi}{2K(k^{-2})} & , r_2 < q < r_3 \end{cases}, \quad (59)$$

$\langle \sin \gamma \sin \alpha \rangle = 0$ ,  $\langle \sin \gamma \cos \gamma \sin \alpha \rangle = 0$ ,  $\langle \sin \gamma \cos \gamma \cos \alpha \rangle = 0$ , and  $\langle \sin^2 \gamma \sin \alpha \cos \alpha \rangle = 0$ . In equations (58) and (59), the + (–) signs are for the positive (negative) flip states with respect to  $\hat{a}_1$  and  $\hat{a}_3$ , respectively. From the definition of  $q$  in equation (1), the expression  $E = \frac{1}{2} \sum_i I_i \omega_i^2$ , and equations (49)–(51),

$$q = \cos^2 \gamma + r_2 \sin^2 \gamma + r_3 \sin^2 \gamma \cos^2 \alpha. \quad (60)$$

Thus, for all values of  $q$ ,

$$r_2 \langle \sin^2 \gamma \sin^2 \alpha \rangle + r_3 \langle \sin^2 \gamma \cos^2 \alpha \rangle = q - \langle \cos^2 \gamma \rangle. \quad (61)$$

This result will be useful in Section 6.

## 6 EXTERNAL PROCESSES

We assume that every gas-phase particle that strikes the grain returns to the gas, via either thermal evaporation or incorporation into an  $\text{H}_2$  molecule that forms on the grain surface and is ejected. We take the arrival and departure rates to be equal and apply a stochastic treatment for these processes. Of the two torques associated with the interstellar magnetic field, the Davis-Greenstein torque is treated deterministically and the Barnett torque is omitted, since it only yields a precession in the angle  $\phi_B$ , which is not relevant for any of the other dynamics under consideration.

### 6.1 Langevin equation

Since the grain rotation time-scale is orders of magnitude smaller than all other relevant time-scales, we average over grain rotation, assuming free rotation, as described in Section 5, as a highly accurate approximation. Thus, at any time  $t$ , the grain is characterized by its angular momentum  $\mathbf{J}$ , rotational kinetic energy  $E$  or its dimensionless measure  $q$ , and flip state (with respect to either  $\hat{\mathbf{a}}_1$  or  $\hat{\mathbf{a}}_3$ , depending on the value of  $q$ ). The time-scale for internal relaxation (i.e. Barnett plus nuclear) is  $\tau_{\text{int}} = (\tau_{\text{Bar}}^{-1} + \tau_{\text{nuc}}^{-1})^{-1}$ , where the Barnett relaxation time-scale  $\tau_{\text{Bar}}$  is found from equation (19) and the nuclear relaxation time-scale is found using equations (17)–(19). Since  $\tau_{\text{int}}$  is orders of magnitude shorter than the time-scales associated with external processes, we neglect the role of external processes in the evolution of the grain’s rotational energy. That is, we simply evolve  $q$  using the Langevin equation (2).

The angular momentum  $\mathbf{J}$  must, of course, be tracked in alignment coordinates, which are fixed in space (see Section 4). However, for the processes with stochastic treatments, it is easier to evaluate the change  $d\mathbf{J}$  in instantaneous angular-momentum coordinates and then transform the result to alignment coordinates. In this manner,  $d\mathbf{J}$  is found from three coupled Langevin equations:

$$dJ_{i,J} = \langle \Gamma_{i,J}(\mathbf{J}, q, \text{fs}) \rangle dt + \sum_{j=1}^3 \langle B_{ij,J}(\mathbf{J}, q, \text{fs}) \rangle dw_{j,J} \quad (i = 1-3) \quad (62)$$

where  $dt$  is the time step and  $dw_{j,J}$  are Gaussian random variables with variance  $dt$ . The subscript ‘ $J$ ’ indicates that quantities are evaluated in angular-momentum coordinates, angle brackets denote averages over grain rotation, ‘fs’ denotes the flip state, which is positive or negative (equations 40, 42, 45, 47), and  $\langle B_{ij,J}(\mathbf{J}, q, \text{fs}) \rangle$  are components of the matrix square root of the rotationally averaged diffusion tensor. The components  $\langle \Gamma_{i,J}(\mathbf{J}, q, \text{fs}) \rangle$  of the rotationally averaged mean torque and the components  $\langle C_{ij,J}(\mathbf{J}, q, \text{fs}) \rangle$  of the rotationally averaged diffusion tensor can depend on  $\mathbf{J}$ ,  $q$ , and the flip state. These quantities are evaluated in the following subsections.

### 6.2 Collisions

Suppose the gas, with temperature  $T_{\text{gas}}$ , consists of particles with mass  $m$  and number density  $n$ . The gas thermal speed is defined as

$$v_{\text{th}} = \left( \frac{2k_B T_{\text{gas}}}{m} \right)^{1/2} \quad (63)$$

where  $k_B$  is Boltzmann’s constant. The velocity of a gas particle  $\mathbf{v} = v_{\text{th}} \mathbf{s}$ . The ‘reduced velocity’  $s$  is characterized by polar angle  $\theta_{\text{in}}$  and azimuthal angle  $\phi_{\text{in}}$ , with  $\hat{\mathbf{N}}$  as the polar axis and  $\hat{\mathbf{t}}$  as the

azimuthal axis (recall equations 25 and 27). Thus,

$$\hat{\mathbf{s}} = - \left( \hat{\mathbf{N}} \cos \theta_{\text{in}} + \hat{\mathbf{t}} \sin \theta_{\text{in}} \cos \phi_{\text{in}} + \hat{\phi}' \sin \theta_{\text{in}} \sin \phi_{\text{in}} \right). \quad (64)$$

The Maxwell velocity distribution is

$$P(s) s^2 ds d\Omega = \pi^{-3/2} \exp(-s^2) s^2 ds d\Omega \quad (65)$$

where  $d\Omega$  is the solid-angle element.

The velocity of the gas particle relative to a patch on the grain surface is

$$\mathbf{V} = v_{\text{th}} s \hat{\mathbf{s}} - \boldsymbol{\omega} \times \mathbf{r} \quad (66)$$

where  $\boldsymbol{\omega}$  is the grain’s angular velocity and  $\mathbf{r}$  is the displacement from the grain’s center of mass to the surface patch, with components given by equations (21)–(23). Thus, the rate at which gas particles with reduced speeds between  $s$  and  $s + ds$  collide with a surface patch with area  $dS$  (equation 24) from within solid angle  $d\Omega = d(\cos \theta_{\text{in}}) d\phi_{\text{in}}$  about the direction characterized by  $(\theta_{\text{in}}, \phi_{\text{in}})$  is

$$dR_{\text{col}} = \pi^{-3/2} n v_{\text{th}} ds s^2 \exp(-s^2) d(\cos \theta_{\text{in}}) d\phi_{\text{in}} V' dS \quad (67)$$

when  $V' > 0$  (and zero otherwise) where

$$V' = \left( s \hat{\mathbf{s}} - \frac{\boldsymbol{\omega} \times \mathbf{r}}{v_{\text{th}}} \right) \cdot (-\hat{\mathbf{N}}). \quad (68)$$

From equations (21)–(23), (25), (49)–(51), and (64),

$$V' = s \cos \theta_{\text{in}} + \frac{J a_{\text{eff}} \delta^{-1/3}}{I_1 v_{\text{th}}} \left( 1 - \delta^2 \right) A(\delta, \eta) \sin \eta \cos \eta \sin \gamma \times (r_2 \sin \phi' \sin \alpha - r_3 \cos \phi' \cos \alpha); \quad (69)$$

$A(\delta, \eta)$  is defined in equation (32).

We assume that  $J a_{\text{eff}} / I_1 v_{\text{th}} \ll 1$ , so the second term in the expression for  $V'$  can be neglected unless the first term yields a zero integral and the lower limit in integrals over  $s$  can simply be taken to be zero.

The angular momentum acquired by the grain when a gas-phase particle collides and sticks to the surface, as observed in an inertial frame, is

$$\Delta \mathbf{J}_{\text{col}} = m v_{\text{th}} s \mathbf{r} \times \hat{\mathbf{s}} = m v_{\text{th}} a_{\text{eff}} \delta^{-1/3} \Delta \mathbf{J}'_{\text{col}}, \quad (70)$$

where, from equations (21)–(23), (25)–(27), and (64),

$$\Delta \mathbf{J}'_{x,\text{col}} = s \left[ -A(\delta, \eta) \left( 1 - \delta^2 \right) \sin \eta \cos \eta \sin \phi' \cos \theta_{\text{in}} + A(\delta, \eta) \delta \sin \phi' \sin \theta_{\text{in}} \cos \phi_{\text{in}} + \delta \sin \eta \cos \phi' \sin \theta_{\text{in}} \sin \phi_{\text{in}} \right], \quad (71)$$

$$\Delta \mathbf{J}'_{y,\text{col}} = s \left[ A(\delta, \eta) \left( 1 - \delta^2 \right) \sin \eta \cos \eta \cos \phi' \cos \theta_{\text{in}} - A(\delta, \eta) \delta \cos \phi' \sin \theta_{\text{in}} \cos \phi_{\text{in}} + \delta \sin \eta \sin \phi' \sin \theta_{\text{in}} \sin \phi_{\text{in}} \right], \quad (72)$$

$$\Delta \mathbf{J}'_{z,\text{col}} = -s \cos \eta \sin \theta_{\text{in}} \sin \phi_{\text{in}}. \quad (73)$$

The mean torque on the grain due to collisions with gas particles is

$$\boldsymbol{\Gamma}_{\text{col}} = \int dR_{\text{col}} \Delta \mathbf{J}_{\text{col}}. \quad (74)$$

From equations (67), (69), (70)–(73), and (74),

$$\Gamma_{\text{col}} = -\frac{\sqrt{\pi}}{2}nmv_{\text{th}}a_{\text{eff}}^4\delta^{-4/3}\left(1-\delta^2\right)^2\mathcal{I}_4(\delta)\frac{\mathbf{J}}{I_1}\sin\gamma \\ \times (r_2\sin\alpha\hat{\mathbf{x}}+r_3\cos\alpha\hat{\mathbf{y}}). \quad (75)$$

From equations (37), (38), and (52), the rotationally averaged torque is

$$\langle\Gamma_{\text{col}}\rangle = -\frac{\sqrt{\pi}}{2}nmv_{\text{th}}a_{\text{eff}}^4\delta^{-4/3}\left(1-\delta^2\right)^2\mathcal{I}_4(\delta)\frac{\mathbf{J}}{I_1} \\ \times (r_2\langle\sin^2\gamma\sin^2\alpha\rangle+r_3\langle\sin^2\gamma\cos^2\alpha\rangle); \quad (76)$$

expressions for  $\mathcal{I}_4(\delta)$  and  $r_2\langle\sin^2\gamma\sin^2\alpha\rangle+r_3\langle\sin^2\gamma\cos^2\alpha\rangle$  are given in equations (31) and (61). Note that  $\langle\Gamma_{\text{col}}\rangle=0$  for steady rotation about the geometric symmetry axis (i.e.  $\gamma=0$ ), in agreement with previous results (Purcell & Spitzer 1971; Roberge et al. 1993).

The diffusion coefficients are given by

$$C_{ij,\text{col}} = \int dR_{\text{col}}\Delta J_{i,\text{col}}\Delta J_{j,\text{col}}. \quad (77)$$

The diffusion tensor in grain-body coordinates is diagonal, with

$$C_{zz,\text{col}} = \frac{2\sqrt{\pi}}{3}nm^2v_{\text{th}}^3a_{\text{eff}}^4\delta^{-4/3}Z_1(\delta), \quad (78)$$

$$C_{xx,\text{col}} = C_{yy,\text{col}} = \frac{2\sqrt{\pi}}{3}nm^2v_{\text{th}}^3a_{\text{eff}}^4\delta^{-4/3}Z_2(\delta), \quad (79)$$

where

$$Z_1(\delta) = \frac{3}{4}[\mathcal{I}_2(\delta)-\mathcal{I}_1(\delta)] = \frac{3}{16}\left[3+4\delta^2g(\delta)-\frac{1-\delta^4g(\delta)}{1-\delta^2}\right] \quad (80)$$

and

$$Z_2(\delta) = \frac{3}{8}\left\{2\left(1-\delta^2\right)^2\mathcal{I}_4(\delta)+\delta^2[\mathcal{I}_1(\delta)+\mathcal{I}_3(\delta)]\right\} \\ = \frac{3}{32}\frac{4-3\delta^4+\delta^4(2-3\delta^2)g(\delta)}{1-\delta^2}. \quad (81)$$

The integrals  $\mathcal{I}_i(\delta)$  and the function  $g(\delta)$  are defined in Section 3. Note that, to within the approximations adopted here,  $C_{zz,\text{col}}$  and  $C_{xx,\text{col}}$  are independent of the grain rotation and that the results in equations (78) and (79) are identical to those found by Roberge et al. (1993).

Transforming the diffusion tensor to angular-momentum coordinates and averaging over grain rotation,

$$\langle C_{zz,J,\text{col}}\rangle = \frac{2\sqrt{\pi}}{3}nm^2v_{\text{th}}^3a_{\text{eff}}^4\delta^{-4/3}\left[Z_1(\delta)\langle\cos^2\gamma\rangle+Z_2(\delta)\langle\sin^2\gamma\rangle\right] \quad (82)$$

and

$$\langle C_{xx,J,\text{col}}\rangle = \langle C_{yy,J,\text{col}}\rangle = \frac{2\sqrt{\pi}}{3}nm^2v_{\text{th}}^3a_{\text{eff}}^4\delta^{-4/3} \\ \times \frac{1}{2}\left[Z_2(\delta)\left(1+\langle\cos^2\gamma\rangle\right)+Z_1(\delta)\langle\sin^2\gamma\rangle\right]. \quad (83)$$

### 6.3 Evaporation

Consider thermal evaporation of particles of mass  $m_{\text{ev}}$ , distributed uniformly across the grain surface. The total evaporation rate must

equal the total collision rate and detailed balancing applies when the evaporation temperature  $T_{\text{ev}}$  equals the gas temperature  $T_{\text{gas}}$ . Thus, as described in Appendix B in Roberge et al. (1993), the rate at which particles evaporate from a surface patch with area  $dS$ , with speeds between  $v_{\text{th,ev}}s$  and  $v_{\text{th,ev}}(s+ds)$  and from within solid angle  $d\Omega = d(\cos\theta_{\text{in}})d\phi_{\text{in}}$  about the direction characterized by  $(\theta_{\text{in}},\phi_{\text{in}})$ , is

$$dR_{\text{ev}} = \pi^{-3/2}\frac{m}{m_{\text{ev}}}nv_{\text{th}}ds^3\exp(-s^2)d(\cos\theta_{\text{in}})\cos\theta_{\text{in}}d\phi_{\text{in}}dS. \quad (84)$$

The evaporative thermal speed  $v_{\text{th,ev}}$  is defined identically to the gas thermal speed, except  $T_{\text{gas}}$  and  $m$  in equation (63) are replaced with  $T_{\text{ev}}$  and  $m_{\text{ev}}$ .

The angular momentum imparted to the grain following an evaporation event is

$$\Delta\mathbf{J}_{\text{ev}} = m_{\text{ev}}\mathbf{r}\times(v_{\text{th,ev}}s\hat{\mathbf{s}}-\boldsymbol{\omega}\times\mathbf{r}) = mv_{\text{th}}a_{\text{eff}}\delta^{-1/3}\Delta\mathbf{J}'_{\text{ev}} \quad (85)$$

where, from equations (21)–(23), (25)–(27), (49)–(51), and (64),

$$\Delta\mathbf{J}'_{\text{ev}} = \Delta\mathbf{J}'_{\text{ev}}(1) + \Delta\mathbf{J}'_{\text{ev}}(2), \quad (86)$$

$$\Delta\mathbf{J}'_{\text{ev}}(1) = \frac{m_{\text{ev}}v_{\text{th,ev}}}{mv_{\text{th}}}\Delta\mathbf{J}'_{\text{col}}, \quad (87)$$

$$\Delta\mathbf{J}'_{x,\text{ev}}(2) = \frac{m_{\text{ev}}}{m}\frac{Ja_{\text{eff}}\delta^{-1/3}}{I_1v_{\text{th}}}\left(r_3\sin\gamma\cos\alpha\cos^2\eta\sin\phi'\cos\phi' \right. \\ \left.-r_2\sin\gamma\sin\alpha\cos^2\eta\sin^2\phi'-\delta^2r_2\sin\gamma\sin\alpha\sin^2\eta \right. \\ \left. +\delta\cos\gamma\sin\eta\cos\eta\cos\phi'\right), \quad (88)$$

$$\Delta\mathbf{J}'_{y,\text{ev}}(2) = \frac{m_{\text{ev}}}{m}\frac{Ja_{\text{eff}}\delta^{-1/3}}{I_1v_{\text{th}}}\left(r_2\sin\gamma\sin\alpha\cos^2\eta\sin\phi'\cos\phi' \right. \\ \left.-r_3\sin\gamma\cos\alpha\cos^2\eta\cos^2\phi'-\delta^2r_3\sin\gamma\cos\alpha\sin^2\eta \right. \\ \left. +\delta\cos\gamma\sin\eta\cos\eta\sin\phi'\right), \quad (89)$$

$$\Delta\mathbf{J}'_{z,\text{ev}}(2) = \frac{m_{\text{ev}}}{m}\frac{Ja_{\text{eff}}\delta^{-1/3}}{I_1v_{\text{th}}}\left[\delta\sin\gamma\sin\eta\cos\eta \right. \\ \left.\times(r_2\sin\alpha\cos\phi'+r_3\cos\alpha\sin\phi')-\cos\gamma\cos^2\eta\right]. \quad (90)$$

Evaluation of the mean torque and diffusion tensor associated with evaporation proceeds in the same way as for collisions, yielding

$$\langle\Gamma_{\text{ev}}\rangle = -\frac{\sqrt{\pi}}{2}nmv_{\text{th}}a_{\text{eff}}^4\delta^{-4/3}\frac{\mathbf{J}}{I_1}\left\{2[\mathcal{I}_2(\delta)-\mathcal{I}_1(\delta)]\langle\cos^2\gamma\rangle+ \right. \\ \left. [\mathcal{I}_2(\delta)-(1-2\delta^2)\mathcal{I}_1(\delta)]\left(r_2\langle\sin^2\gamma\sin^2\alpha\rangle+r_3\langle\sin^2\gamma\cos^2\alpha\rangle\right)\right\} \quad (91)$$

and

$$C_{ij,\text{ev}} = \frac{T_{\text{ev}}}{T_{\text{gas}}}C_{ij,\text{col}}. \quad (92)$$

The prefactor in equation (92) results as follows:  $C_{ij,\text{col}} \propto m^2v_{\text{th}}^3$  and  $C_{ij,\text{ev}} \propto mm_{\text{ev}}v_{\text{th}}v_{\text{th,ev}}^2$ , so  $C_{ij,\text{ev}}/C_{ij,\text{col}} = m_{\text{ev}}v_{\text{th,ev}}^2/(mv_{\text{th}}^2) = T_{\text{ev}}/T_{\text{gas}}$ . When  $r_2=r_3$  and  $\gamma=0$ , equations (91) and (92) reduce to equations C17 and C21 in Roberge et al. (1993) for the mean torque and diffusion tensor for an oblate spheroid with dynamic symmetry rotating steadily about the symmetry axis.

#### 6.4 Formation and ejection of H<sub>2</sub>

Now consider the case that particles depart the grain as newly formed H<sub>2</sub> molecules. For simplicity, we will assume that the molecules have a fixed kinetic energy  $E_{\text{H}_2}$ . With  $m_{\text{H}_2} = 2m$ , the departure speed is  $v_{\text{H}_2} = (2E_{\text{H}_2}/m_{\text{H}_2})^{1/2}$ . For convenience, define  $T_{\text{H}_2} = E_{\text{H}_2}/k_B$ .

##### 6.4.1 Uniformly distributed formation sites

First suppose that the formation sites fully cover the grain surface, with a fixed number density per unit surface area. If the departing molecules are distributed uniformly in solid angle, then the analysis in Section 6.3 applies with minor modification. Integrating equation (84) over  $s$ , the departure rate from a surface patch is

$$dR_{\text{H}_2} = \frac{\pi^{-3/2}}{2} \frac{m}{m_{\text{H}_2}} n v_{\text{th}} d(\cos \theta_{\text{in}}) \cos \theta_{\text{in}} d\phi_{\text{in}} dS. \quad (93)$$

The angular momentum imparted to the grain when an H<sub>2</sub> molecule departs is identical to that in equation (85) except that  $m_{\text{ev}}$  is replaced with  $m_{\text{H}_2}$  and  $v_{\text{th, ev}}$   $s$  is replaced with  $v_{\text{H}_2}$ . Thus,

$$\Delta \mathbf{J}'_{\text{H}_2} = \Delta \mathbf{J}'_{\text{H}_2}(1) + \Delta \mathbf{J}'_{\text{H}_2}(2), \quad (94)$$

where the components of  $\Delta \mathbf{J}'_{\text{H}_2}(2)$  are given by equations (88)–(90), except with  $m_{\text{ev}}$  replaced by  $m_{\text{H}_2}$ , and  $\Delta \mathbf{J}'_{\text{H}_2}(1)$  is given by equation (87), except with  $m_{\text{ev}} v_{\text{th, ev}}$  replaced by  $m_{\text{H}_2} v_{\text{H}_2}/s$ . In evaluating the mean torque, the term involving  $\Delta \mathbf{J}'_{\text{H}_2}(1)$  vanishes upon integration. Thus,

$$\langle \Gamma_{\text{H}_2} \rangle = \langle \Gamma_{\text{ev}} \rangle. \quad (95)$$

With the assumption that  $Ja_{\text{eff}}/I_1 v_{\text{th}} \ll 1$ , only the term involving  $\Delta \mathbf{J}'_{\text{H}_2}(1)$  contributes to the diffusion tensor. In the calculation of  $C_{ij, \text{ev}}$ , a term  $\int_0^\infty ds s^5 \exp(-s^2)$  arises. This term evaluates to unity and is replaced by the factor  $\frac{1}{2}$  in equation (93) in the calculation of  $C_{ij, \text{H}_2}$ . Thus,

$$\frac{C_{ij, \text{H}_2}}{C_{ij, \text{ev}}} = \frac{\frac{1}{2} m m_{\text{H}_2} v_{\text{th}} v_{\text{H}_2}^2}{m m_{\text{ev}} v_{\text{th}} v_{\text{th, ev}}^2}. \quad (96)$$

Finally,

$$C_{ij, \text{H}_2} = \frac{1}{2} \frac{T_{\text{H}_2}}{T_{\text{ev}}} C_{ij, \text{ev}} = \frac{1}{2} \frac{T_{\text{H}_2}}{T_{\text{gas}}} C_{ij, \text{col}}. \quad (97)$$

##### 6.4.2 Special formation sites

Now consider a grain where H<sub>2</sub> formation only occurs at a set of  $N_s$  special surface sites. We randomly select the position  $(\eta_i, \phi'_i)$  of each site from a uniform distribution (in surface area) over the surface. From equation (24), the surface area element is

$$dS = a_{\text{eff}}^2 \delta^{-2/3} du d\phi' \quad (98)$$

with

$$du = \left[ \delta^2 + (1 - \delta^2) \sin^2 \eta \right]^{1/2} \cos \eta d\eta. \quad (99)$$

Thus, for each site  $\phi'_i$  is selected randomly from a uniform distribution in  $\phi'$  (0 to  $2\pi$ ) and  $\eta_i$  is selected randomly from a uniform

distribution in  $u$ , where  $u$  and  $\eta$  are related by

$$u = \frac{1}{2} \left[ 1 + \sin \eta \sqrt{\delta^2 + (1 - \delta^2) \sin^2 \eta} \right] + \frac{\delta^2}{2\sqrt{1 - \delta^2}} \times \left\{ \ln \left[ \left( 1 + \sqrt{1 - \delta^2} \right) \left( \sqrt{1 - \delta^2} \sin \eta + \sqrt{\delta^2 + (1 - \delta^2) \sin^2 \eta} \right) \right] - 2 \ln \delta \right\}. \quad (100)$$

As  $\eta$  ranges from  $-\pi/2$  to  $\pi/2$ ,  $u$  ranges from 0 to

$$u_{\text{max}} = 1 + \frac{\delta^2}{\sqrt{1 - \delta^2}} \ln \left( \frac{1 + \sqrt{1 - \delta^2}}{\delta} \right) = 1 + \delta^2 g(\delta). \quad (101)$$

We will assume that molecule formation occurs at the same rate at each surface site. Thus, the rate per site at which molecules are ejected is

$$R_{\text{H}_2}(\text{per site}) = \frac{R_{\text{col}}}{2N_s}, \quad (102)$$

where  $R_{\text{col}}$  is the total rate at which gas atoms collide with the grain and the factor of  $\frac{1}{2}$  appears since there are 2 H atoms per H<sub>2</sub> molecule. From equations (67), (69), (24), and (29),

$$R_{\text{col}} = \sqrt{\pi} n v_{\text{th}} a_{\text{eff}}^2 \delta^{-2/3} \left[ 1 + \delta^2 g(\delta) \right]. \quad (103)$$

A systematic torque only has the potential to maintain suprathermal grain rotation if it has a non-zero component along  $\hat{\mathbf{z}} = \hat{\mathbf{a}}_1$ . Otherwise, from equations (37) and (38), the component of the rotationally averaged systematic torque along  $\hat{\mathbf{J}} = \hat{\mathbf{z}}_J$  vanishes in the limit  $\gamma \rightarrow 0$ , which characterizes suprathermal rotation. From equation (73), the component of the torque along  $\hat{\mathbf{z}}$  vanishes if the outgoing molecules are uniformly distributed in solid angle, or if they depart along the surface normal  $\hat{\mathbf{N}}$ . This is a consequence of the spheroidal shape, for which the components of  $\mathbf{r}$  (the displacement from the grain center to the surface patch) and  $\hat{\mathbf{N}}$  that are perpendicular to  $\hat{\mathbf{z}}$  lie in the same direction, so that  $\mathbf{r} \times \hat{\mathbf{N}}$  has zero component along  $\hat{\mathbf{z}}$ . So rather than taking the outgoing molecules to be uniformly distributed in solid angle, we randomly pick angles  $\theta_{\text{out}, i}$  (from a uniform distribution in  $\cos^2 \theta_{\text{out}}$  between  $[(\cos \theta_{\text{out}})_{\text{min}}]^2$  and 1) and  $\phi_{\text{out}, i}$  (uniformly distributed between 0 and  $2\pi$ ) for each site such that a molecule departing site  $i$  has velocity

$$v_{\text{H}_2} = v_{\text{H}_2} \left( \hat{\mathbf{N}}_i \cos \theta_{\text{out}, i} + \hat{\mathbf{t}}_i \sin \theta_{\text{out}, i} \cos \phi_{\text{out}, i} + \hat{\phi}'_i \sin \theta_{\text{out}, i} \sin \phi_{\text{out}, i} \right). \quad (104)$$

The form of the distribution for  $\theta_{\text{out}, i}$  was chosen for consistency with the treatment of the case with uniformly distributed formation sites. In our simulations, we adopt  $(\cos \theta_{\text{out}})_{\text{min}} = 0.8$ .

In contrast to the case where the surface is uniformly covered with H<sub>2</sub>-formation sites, the mean torque associated with  $\Delta \mathbf{J}'_{\text{H}_2}(1)$  does not vanish. This term accounts for the systematic torque, while the term associated with  $\Delta \mathbf{J}'_{\text{H}_2}(2)$  combines with the torque due to collisions with atoms to account for the drag torque. The mean systematic torque is

$$\Gamma_{\text{H}_2, \text{sys}} = R_{\text{H}_2}(\text{per site}) \sum_{i=1}^{N_s} \Delta \mathbf{J}_{\text{H}_2}(1)_i. \quad (105)$$

The rotationally averaged systematic torque is

$$\langle \Gamma_{\text{H}_2, \text{sys}} \rangle = \sqrt{\pi} m n v_{\text{th}} v_{\text{H}_2} a_{\text{eff}}^3 \delta^{-1} \left[ 1 + \delta^2 g(\delta) \right] \times (Q_1 \langle \cos \gamma \rangle + Q_2 \langle \sin \gamma \cos \alpha \rangle) \hat{\mathbf{J}}, \quad (106)$$



where

$$Q_1 = -\frac{1}{N_s} \sum_{i=1}^{N_s} \cos \eta_i \sin \theta_{\text{out},i} \sin \phi_{\text{out},i}, \quad (107)$$

$$Q_2 = \frac{1}{N_s} \sum_{i=1}^{N_s} \left[ \left( (1 - \delta^2) A(\delta, \eta_i) \sin \eta_i \cos \eta_i \cos \phi'_i \cos \theta_{\text{out},i} \right. \right. \\ \left. \left. - \delta A(\delta, \eta_i) \cos \phi'_i \sin \theta_{\text{out},i} \cos \phi_{\text{out},i} \right. \right. \\ \left. \left. + \delta \sin \eta_i \sin \phi'_i \sin \theta_{\text{out},i} \sin \phi_{\text{out},i} \right], \quad (108)$$

and  $\langle \cos \gamma \rangle$  and  $\langle \sin \gamma \cos \alpha \rangle$  are evaluated in equations (58) and (59).

The contribution to the drag torque is evaluated similarly, except that  $\Delta \mathbf{J}_{\text{H}_2}(1)$  is replaced with  $\Delta \mathbf{J}_{\text{H}_2}(2)$ . After some algebra, we find that

$$\langle \Gamma_{\text{H}_2, \text{drag}} \rangle = -\sqrt{\pi} m n v_{\text{th}} a_{\text{eff}}^4 \delta^{-4/3} \left[ 1 + \delta^2 g(\delta) \right] \frac{\mathbf{J}}{I_1} \\ \times \left( Q_3 \langle \cos^2 \gamma \rangle + Q_4 \langle \sin^2 \gamma \sin^2 \alpha \rangle + Q_5 \langle \sin^2 \gamma \cos^2 \alpha \rangle \right), \quad (109)$$

where

$$Q_3 = \frac{1}{N_s} \sum_{i=1}^{N_s} \cos^2 \eta_i, \quad (110)$$

$$Q_4 = \frac{r_2}{N_s} \sum_{i=1}^{N_s} \left( \cos^2 \eta_i \sin^2 \phi'_i + \delta^2 \sin^2 \eta_i \right), \quad (111)$$

$$Q_5 = \frac{r_3}{N_s} \sum_{i=1}^{N_s} \left( \cos^2 \eta_i \cos^2 \phi'_i + \delta^2 \sin^2 \eta_i \right), \quad (112)$$

and  $\langle \cos^2 \gamma \rangle$ ,  $\langle \sin^2 \gamma \sin^2 \alpha \rangle$ , and  $\langle \sin^2 \gamma \cos^2 \alpha \rangle$  are evaluated in equations (53), (56), and (57). In the limit of uniform surface coverage of  $\text{H}_2$ -formation sites, equation (109) reproduces equation (95).

The diffusion tensor in grain-body coordinates is given by

$$C_{ij, \text{H}_2} = 2\sqrt{\pi} m^2 v_{\text{th}}^2 a_{\text{eff}}^4 \delta^{-4/3} \left[ 1 + \delta^2 g(\delta) \right] \\ \times \frac{1}{N_s} \sum_{\rho=1}^{N_s} \Delta \tilde{J}_{\text{H}_2, i}(1)_\rho \Delta \tilde{J}_{\text{H}_2, j}(1)_\rho, \quad (113)$$

where

$$\Delta \tilde{J}_{\text{H}_2, x}(1)_\rho = -A(\delta, \eta_\rho) \left( 1 - \delta^2 \right) \sin \eta_\rho \cos \eta_\rho \sin \phi'_\rho \cos \theta_{\text{out},\rho} \\ + A(\delta, \eta_\rho) \delta \sin \phi'_\rho \sin \theta_{\text{out},\rho} \cos \phi_{\text{out},\rho} \\ + \delta \sin \eta_\rho \cos \phi'_\rho \sin \theta_{\text{out},\rho} \sin \phi_{\text{out},\rho}, \quad (114)$$

$$\Delta \tilde{J}_{\text{H}_2, y}(1)_\rho = A(\delta, \eta_\rho) \left( 1 - \delta^2 \right) \sin \eta_\rho \cos \eta_\rho \cos \phi'_\rho \cos \theta_{\text{out},\rho} \\ - A(\delta, \eta_\rho) \delta \cos \phi'_\rho \sin \theta_{\text{out},\rho} \cos \phi_{\text{out},\rho} \\ + \delta \sin \eta_\rho \sin \phi'_\rho \sin \theta_{\text{out},\rho} \sin \phi_{\text{out},\rho}, \quad (115)$$

$$\Delta \tilde{J}_{\text{H}_2, z}(1)_\rho = -\cos \eta_\rho \sin \theta_{\text{out},\rho} \sin \phi_{\text{out},\rho}. \quad (116)$$

Transforming to angular-momentum coordinates and averaging over grain rotation,

$$\langle C_{xx, J, \text{H}_2} \rangle = \langle C_{yy, J, \text{H}_2} \rangle = \frac{1}{2} C_{xx, \text{H}_2} \left( 1 - \langle \sin^2 \gamma \sin^2 \alpha \rangle \right) \\ + \frac{1}{2} C_{yy, \text{H}_2} \left( 1 - \langle \sin^2 \gamma \cos^2 \alpha \rangle \right) + \frac{1}{2} C_{zz, \text{H}_2} \langle \sin^2 \gamma \rangle, \quad (117)$$

$$\langle C_{zz, J, \text{H}_2} \rangle = C_{xx, \text{H}_2} \langle \sin^2 \gamma \sin^2 \alpha \rangle + C_{yy, \text{H}_2} \langle \sin^2 \gamma \cos^2 \alpha \rangle \\ + C_{zz, \text{H}_2} \langle \cos^2 \gamma \rangle, \quad (118)$$

and the off-diagonal elements all vanish. If  $C_{xx, \text{H}_2} = C_{yy, \text{H}_2}$ , then equations (117) and (118) adopt the form of equations (83) and (82). Since only the three diagonal element of  $C_{ij, \text{H}_2}$  are needed, we define three additional dimensionless efficiency factors,

$$Q_6 = \frac{1}{N_s} \sum_{\rho=1}^{N_s} \left[ \Delta \tilde{J}_{\text{H}_2, x}(1)_\rho \right]^2, \quad (119)$$

$$Q_7 = \frac{1}{N_s} \sum_{\rho=1}^{N_s} \left[ \Delta \tilde{J}_{\text{H}_2, y}(1)_\rho \right]^2, \quad (120)$$

$$Q_8 = \frac{1}{N_s} \sum_{\rho=1}^{N_s} \left[ \Delta \tilde{J}_{\text{H}_2, z}(1)_\rho \right]^2. \quad (121)$$

From equation (113),  $C_{xx, \text{H}_2} \propto Q_6$ ,  $C_{yy, \text{H}_2} \propto Q_7$ , and  $C_{zz, \text{H}_2} \propto Q_8$ .

## 6.5 Davis-Greenstein Torque

Davis & Greenstein (1951) evaluated the rotation-averaged torque due to paramagnetic dissipation in the interstellar magnetic field for the case of an oblate grain with dynamic symmetry:

$$\langle \Gamma_{\text{DG}} \rangle = -\tau_{\text{DG}}^{-1} \left[ 1 + (r_2 - 1) \sin^2 \gamma \right] \left( J_{x, B} \hat{\mathbf{x}}_B + J_{y, B} \hat{\mathbf{y}}_B \right), \quad (122)$$

where the Davis-Greenstein timescale is

$$\tau_{\text{DG}} = \frac{2\alpha_1 \bar{\rho} a_{\text{eff}}^2}{5\chi_0 T_2 B^2} \\ \approx 1.52 \times 10^6 \text{ yr} \left( \frac{\alpha_1 \bar{\rho}}{3 \text{ g cm}^{-3}} \right) \left( \frac{a_{\text{eff}}}{0.1 \mu\text{m}} \right)^2 \left( \frac{T_d}{15 \text{ K}} \right) \left( \frac{B}{5 \mu\text{G}} \right)^{-2}. \quad (123)$$

We assume that for electron paramagnetism,  $\chi''/\omega = \chi_0 T_2 = 10^{-13} (T_d/15 \text{ K})^{-1} \text{ s}$ , where  $\chi''$  is the imaginary component of the magnetic susceptibility. Recall that  $\gamma$  is constant for a freely rotating grain with dynamic symmetry. Rather than attempt a detailed analysis of the torque for the case of a grain lacking dynamic symmetry, we simply adopt the Davis-Greenstein result in equation (122), replacing  $\sin^2 \gamma$  with  $\langle \sin^2 \gamma \rangle$ .

## 7 SIMULATIONS

In this section, we describe the fundamental elements of the simulation codes used in this work.

### 7.1 Dimensionless variables

For numerical integration of the equations of motion, we adopt dimensionless variables

$$J' = \frac{J}{I_1 \omega_T} \quad (124)$$

and

$$t' = \frac{t}{\tau_{\text{drag}}}, \quad (125)$$

where the thermal rotation rate is

$$\begin{aligned} \omega_T &= \left( \frac{15kT_{\text{gas}}}{8\pi\bar{\rho}a_{\text{eff}}^5} \right)^{1/2} \\ &= 1.6573 \times 10^5 \left( \frac{\bar{\rho}}{3 \text{ g cm}^{-3}} \right)^{-1/2} \left( \frac{T_{\text{gas}}}{100 \text{ K}} \right)^{1/2} \left( \frac{a_{\text{eff}}}{0.1 \mu\text{m}} \right)^{-5/2} \text{ s}^{-1} \end{aligned} \quad (126)$$

and the drag time-scale is

$$\begin{aligned} \tau_{\text{drag}} &= \frac{3I_1 \delta^{4/3}}{4\sqrt{\pi} m n v_{\text{th}} a_{\text{eff}}^4} = 1.045 \times 10^5 \alpha_1 \delta^{4/3} \\ &\times \left( \frac{\bar{\rho}}{3 \text{ g cm}^{-3}} \right) \left( \frac{a_{\text{eff}}}{0.1 \mu\text{m}} \right) \left( \frac{n}{30 \text{ cm}^{-3}} \right)^{-1} \left( \frac{T_{\text{gas}}}{100 \text{ K}} \right)^{-1/2} \text{ yr}. \end{aligned} \quad (127)$$

### 7.2 Internal relaxation

In dimensionless variables, the Langevin equation for internal relaxation becomes

$$dq = -A_1(J', q) \frac{\tau_{\text{drag}}}{\tau_{\text{int}}(J')} dt' + B_1[b(J'), q] \sqrt{\frac{\tau_{\text{drag}}}{\tau_{\text{int}}(J')}} dw'_{\text{int}} \quad (128)$$

where  $dw'_{\text{int}}$  is a Gaussian random variable with variance  $dt'$ ,

$$A_1(J', q) = -\tau_{\text{int}}(J') A(q), \quad (129)$$

and

$$B_1[b(J'), q] = \sqrt{\tau_{\text{int}}(J') D[b(J'), q]}. \quad (130)$$

Random numbers and Gaussian random variables are computed using modified versions of the routines `RAN2` and `GASDEV` from [Press et al. \(1992\)](#). The internal drift and diffusion coefficients  $A_1(q)$  and  $B_1(b, q)$  are computed using equations (55), (61), and (81) in [Kolasi & Weingartner \(2017\)](#), adopting their assumption that  $D[b(J'), q] = 0$  when  $q = r_3$ . The function  $b(J')$  is defined by

$$b(J') = \frac{J^2}{2I_1 k T_d} = \frac{\alpha_1}{2} \frac{T_{\text{gas}}}{T_d} (J')^2. \quad (131)$$

From the final two paragraphs in Section 2, we take

$$\tau_{\text{int}}(J') = \left\{ [\tau_{\text{Bar}}(J')]^{-1} + [\tau_{\text{nuc}}(J')]^{-1} \right\}^{-1}, \quad (132)$$

$$\begin{aligned} \tau_{\text{Bar}}(J') &= 6.77 \times 10^6 \alpha_1 \left( \frac{\bar{\rho}}{3 \text{ g cm}^{-3}} \right)^2 \left( \frac{a_{\text{eff}}}{0.1 \mu\text{m}} \right)^7 \left( \frac{T_{\text{gas}}}{100 \text{ K}} \right)^{-1} \\ &\times \left( \frac{T_d}{15 \text{ K}} \right) (J')^{-2} \text{ s}, \end{aligned} \quad (133)$$

$$\begin{aligned} \tau_{\text{nuc}}(J') &= 1.36 \times 10^{-5} \tau_{\text{Bar}}(J') \left\{ 1 + 410 \left[ \left( \frac{\bar{\rho}}{3 \text{ g cm}^{-3}} \right)^{-1/2} \right. \right. \\ &\times \left. \left. \left( \frac{T_{\text{gas}}}{100 \text{ K}} \right)^{1/2} \left( \frac{a_{\text{eff}}}{0.1 \mu\text{m}} \right)^{-5/2} \right]^{1.96} (J')^{1.96} \right\}^{1.02}. \end{aligned} \quad (134)$$

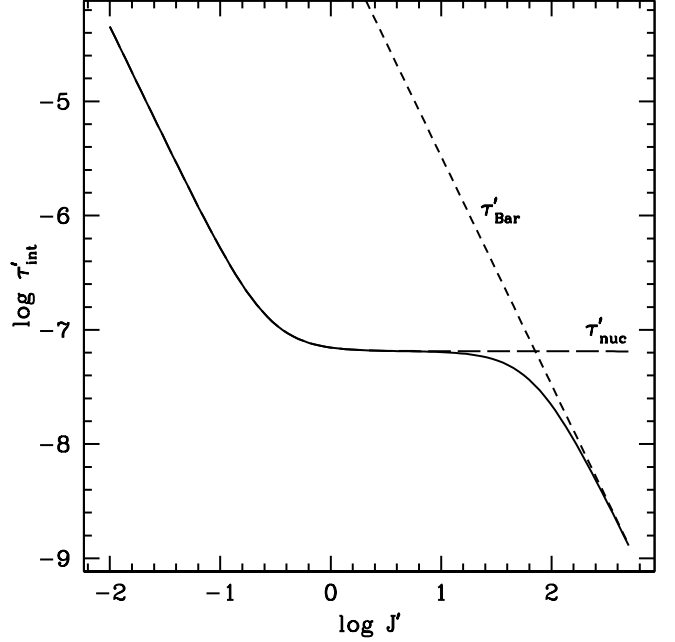


**Figure 1.** Internal relaxation times normalized to the drag time, from equations (132)–(134), for  $r_2 = 1.3$ ,  $r_3 = 1.5$ ,  $\bar{\rho} = 3 \text{ g cm}^{-3}$ ,  $T_{\text{gas}} = 100 \text{ K}$ ,  $T_d = 15 \text{ K}$ , and  $a_{\text{eff}} = 0.2 \mu\text{m}$ .

Fig. 1 shows the internal relaxation times from the above three equations versus  $J'$ , adopting parameter values suitable for a silicate grain in the cold neutral medium (CNM):  $r_2 = 1.3$ ,  $r_3 = 1.5$ ,  $\bar{\rho} = 3 \text{ g cm}^{-3}$ ,  $T_{\text{gas}} = 100 \text{ K}$ ,  $T_d = 15 \text{ K}$ , and  $a_{\text{eff}} = 0.2 \mu\text{m}$ . (Throughout this paper, we will denote the base-10 logarithm by ‘log’ and the natural logarithm by ‘ln’.) When following the evolution of  $q$  in simulations, we must ensure that the time step size  $dt' \ll \tau'_{\text{int}}$ .

We construct interpolation tables for  $A_1(q)$  and  $B_1(b, q)$ , using `MATHEMATICA`. As seen in Fig. 1 in [Kolasi & Weingartner \(2017\)](#), these functions approach zero very steeply at  $q = r_2$ . They also approach zero at  $q = r_3$ , as does  $A(q)$  at  $q = 1$ . In order to obtain precise values of  $A_1(q)$  and  $B_1(b, q)$  for all  $q$ , we construct tables for  $B_1(b, q)$  for six separate ranges of  $q$ : (1)  $q \in [1 + 10^{-15}, 1.01]$  with uniform spacing in  $\ln(q-1)$ , (2)  $q \in [1.01, 1.28]$  with uniform spacing in  $q$ , (3)  $q \in [1.28, 1.3 - 10^{-15}]$  (recall that  $r_2 = 1.3$ ) with uniform spacing in  $\ln(r_2 - q)$ , (4)  $q \in [1.3 + 10^{-15}, 1.32]$  with uniform spacing in  $\ln(q - r_2)$ , (5)  $q \in [1.32, 1.49]$  with uniform spacing in  $q$ , (6)  $q \in [1.49, 1.5 - 10^{-15}]$  (recall that  $r_3 = 1.5$ ) with uniform spacing in  $\ln(r_3 - q)$ . For each range, we take 2000 values of  $q$ . We take 451 values of  $b$ , spaced uniformly in  $\ln b$ , from  $b_{\text{min}} = 4.45 \times 10^{-10}$  to  $b_{\text{max}} = 5 \times 10^5$ . As seen in equation (81) in [Kolasi & Weingartner \(2017\)](#),  $B_1(b, q)$  becomes independent of  $b$  as  $b \rightarrow 0$ . Thus, for  $b < b_{\text{min}}$ , the minimum value of  $b$  in the interpolation tables, we simply take  $b = b_{\text{min}}$ . Over the full range of  $q$ , the fractional error due to this approximation is always  $< 10^{-10}$ .

We also construct interpolation tables for  $A_1(q)$  in ranges (2)–(5). For  $A_1(q)$  in ranges (1) and (6), we employ the asymptotic formulas in [Kolasi & Weingartner \(2017\)](#), their equations (59) and (62). These are modified slightly as  $q$  deviates from 1 and  $r_3$  to ensure that the asymptotic formulas yield exactly the same result as the interpolation table when  $q = 1.01$  and  $q = 1.49$ , which are the

(1)–(2) and (5)–(6) boundaries, respectively. Thus, we take

$$A_1(q) = c_{A<} (q - 1) [1 - \nu_{<}(q - 1)] \quad , \quad q < 1.01 \quad (135)$$

and

$$A_1(q) = c_{A>} (r_3 - q) [1 - \nu_{>}(r_3 - q)] \quad , \quad q > 1.49 \quad (136)$$

with

$$c_{A<} = \frac{r_3^2(r_2 - 1) + r_2^2(r_3 - 1)}{2}, \quad (137)$$

$$c_{A>} = \frac{r_3 - r_2 + r_2^2(r_3 - 1)}{2}, \quad (138)$$

$$\nu_{<} = 100 \left[ 1 - \frac{100A_1(q = 1.01)}{c_{A<}} \right], \quad (139)$$

and

$$\nu_{>} = 100 \left[ 1 - \frac{100A_1(q = 1.49)}{c_{A>}} \right]. \quad (140)$$

These expressions are exact when  $q = 1.01$  and  $1.49$  and have fractional errors less than  $3 \times 10^{-6}$  in range (1) and  $2 \times 10^{-5}$  in range (6).

Lacking a first-principles theory of Barnett relaxation, it is not clear how to treat the boundaries at  $q = 1$  and  $q = r_3$ . In test runs, we found frequent overshooting of  $q = 1$  (where the diffusion coefficient is non-zero) but not of  $q = r_3$  (where the diffusion coefficient is taken to be zero). In test simulations assuming thermal equilibrium, we found that the distribution function for  $q$  resulting from the simulation best agrees with the theoretical distribution if a ‘reflecting’ boundary condition is adopted at  $q = 1$ . That is, if the value of  $q$  resulting from the Langevin equation is  $1 - \epsilon$ , then we instead set  $q = 1 + \epsilon$ . The treatment of the boundary at  $q = r_3$  does not significantly affect the results. Thus, we adopt ‘reflecting’ boundary conditions at both  $q = 1$  and  $q = r_3$ . In contrast, Weingartner (2009) and Kolasi & Weingartner (2017) reduced the time step and repeated the step whenever the simulation overshoot  $q = 1$ . Since this prescription involves discarding randomly chosen variables, it can introduce statistical biases. Thus, we reject that prescription here.

### 7.3 Angular momentum evolution

In dimensionless variables, the Langevin equations for the grain’s angular-momentum components become

$$dJ'_{i,J} = \langle \Gamma'_{i,J}(\mathbf{J}', q, \text{fs}) \rangle dt' + \sum_{j=1}^3 \langle B'_{ij,J}(\mathbf{J}', q, \text{fs}) \rangle dw'_{j,J} \quad (i = 1-3), \quad (141)$$

where  $dw'_{j,J}$  are Gaussian random variables with variance  $dt'$ ,

$$\langle \Gamma'_{i,J}(\mathbf{J}', q, \text{fs}) \rangle = \frac{\tau_{\text{drag}} \langle \Gamma_{i,J}(\mathbf{J}', q, \text{fs}) \rangle}{I_1 \omega_T}, \quad (142)$$

$$\langle B'_{ij,J}(\mathbf{J}', q, \text{fs}) \rangle = \frac{\tau_{\text{drag}}^{1/2} \langle B_{ij,J}(\mathbf{J}', q, \text{fs}) \rangle}{I_1 \omega_T}, \quad (143)$$

and  $\langle \Gamma_{i,J}(\mathbf{J}', q, \text{fs}) \rangle$  and  $\langle B_{ij,J}(\mathbf{J}', q, \text{fs}) \rangle$  are the components of the rotationally averaged mean torque and diffusion tensor resulting from all of the external processes under consideration, respectively.

In the following sections, we will assume that all of the particles departing the grain surface do so either via thermal evaporation or within  $\text{H}_2$  molecules formed at special surface sites.

### 7.4 Collisions and thermal evaporation

First consider the case that all of the particles departing the grain surface do so via thermal evaporation. From equations (76), (91), (61), (28), (29), (31), and (142), the dimensionless rotationally averaged mean torque, arising from both collisions and evaporation, is given by

$$\begin{aligned} \langle \mathbf{\Gamma}' \rangle_{\text{col+ev}} &= \langle \mathbf{\Gamma}'_{\text{col}} \rangle + \langle \mathbf{\Gamma}'_{\text{ev}} \rangle \\ &= - \left[ Z_1(\delta) \langle \cos^2 \gamma \rangle + Z_2(\delta) (q - \langle \cos^2 \gamma \rangle) \right] \mathbf{J}', \end{aligned} \quad (144)$$

where  $Z_1(\delta)$  and  $Z_2(\delta)$  are defined in equations (80) and (81), respectively. Note that  $Z_1(\delta) \rightarrow 1$  and  $Z_2(\delta) \rightarrow 1$  as  $\delta \rightarrow 1$  (i.e. as the spheroid approaches a sphere). Thus,  $\langle \mathbf{\Gamma}' \rangle = -\mathbf{J}'$  for a sphere, motivating the definition of the drag time-scale in equation (127).

From equations (82), (83), (92), and (143), the dimensionless rotationally averaged diffusion tensor, arising from both collisions and evaporation, is given by

$$\langle C'_{zz,J} \rangle_{\text{col+ev}} = \alpha_1^{-1} \left( 1 + \frac{T_{\text{ev}}}{T_{\text{gas}}} \right) \left[ Z_1(\delta) \langle \cos^2 \gamma \rangle + Z_2(\delta) \langle \sin^2 \gamma \rangle \right], \quad (145)$$

$$\begin{aligned} \langle C'_{xx,J} \rangle_{\text{col+ev}} &= \langle C'_{yy,J} \rangle_{\text{col+ev}} \\ &= \alpha_1^{-1} \left( 1 + \frac{T_{\text{ev}}}{T_{\text{gas}}} \right) \frac{1}{2} \left[ Z_2(\delta) (1 + \langle \cos^2 \gamma \rangle) + Z_1(\delta) \langle \sin^2 \gamma \rangle \right]. \end{aligned} \quad (146)$$

For thermal equilibrium,  $T_{\text{ev}} = T_{\text{gas}}$ .

Roberge & Lazarian (1999) derived the mean torque and diffusion coefficients due to collisions and evaporation for an oblate spheroid with dynamic symmetry. They presented results in an inertial frame, corresponding to our alignment coordinates. With  $T_{\text{ev}} = T_d$  and  $r_2 = r_3$ , our expressions (equations 144–146, with the diffusion tensor transformed from angular-momentum to alignment coordinates using equations 34–36) reduce to the Roberge & Lazarian (1999) expressions (their equations A10–A17). Note that our  $Z_1(\delta)$  and  $Z_2(\delta)$  correspond to their functions  $\Gamma_{\parallel}(e)$  and  $\Gamma_{\perp}(e)$ , respectively. Note also that they define their dimensionless quantities somewhat differently than we do, so that the ratio of our dimensionless mean torque to theirs equals  $Z_1(\delta)$  and the ratio of our dimensionless diffusion tensor components to theirs equals  $Z_1(\delta)/\alpha_1$ .

### 7.5 Collisions and $\text{H}_2$ formation at special sites

Now consider the case that all of the particles departing the grain surface do so within  $\text{H}_2$  molecules formed at special surface sites. From equations (76), (106), and (109), the dimensionless systematic and drag torques are

$$\begin{aligned} \langle \mathbf{\Gamma}'_{\text{H}_2, \text{sys}} \rangle &= \frac{3\nu_{\text{H}_2}}{4a_{\text{eff}} \omega_T} \delta^{1/3} \left[ 1 + \delta^2 g(\delta) \right] \\ &\quad \times (Q_1 \langle \cos \gamma \rangle + Q_2 \langle \sin \gamma \cos \alpha \rangle) \hat{\mathbf{J}}, \end{aligned} \quad (147)$$

$$\begin{aligned}
 \langle \mathbf{\Gamma}'_{\text{drag}} \rangle_{\text{col+H2}} &= \langle \mathbf{\Gamma}'_{\text{col}} \rangle + \langle \mathbf{\Gamma}'_{\text{H2,drag}} \rangle = \\
 &= -\frac{3}{8} J' \hat{\mathbf{J}} \left[ (1 - \delta^2)^2 \mathcal{I}_4(\delta) q + \left\{ 2 \left[ 1 + \delta^2 g(\delta) \right] \mathcal{Q}_3 - (1 - \delta^2)^2 \mathcal{I}_4(\delta) \right\} \right. \\
 &\times \langle \cos^2 \gamma \rangle + 2 \left[ 1 + \delta^2 g(\delta) \right] \left( \mathcal{Q}_4 \langle \sin^2 \gamma \sin^2 \alpha \rangle \right. \\
 &\quad \left. \left. + \mathcal{Q}_5 \langle \sin^2 \gamma \cos^2 \alpha \rangle \right) \right]. \quad (148)
 \end{aligned}$$

From equations (117) and (118), only the diagonal elements of  $C_{ij,\text{H2}}$  are needed. From equation (113),

$$C'_{xx,\text{H2}} = \frac{3mv_{\text{H2}}^2}{2k_B T_{\text{gas}}} \alpha_1^{-1} \left[ 1 + \delta^2 g(\delta) \right] \mathcal{Q}_6; \quad (149)$$

$C'_{yy,\text{H2}}$  and  $C'_{zz,\text{H2}}$  are of identical form, with  $\mathcal{Q}_6$  replaced by  $\mathcal{Q}_7$  and  $\mathcal{Q}_8$ , respectively. The components of the dimensionless rotationally averaged diffusion tensor for collisions are given in equations (145) and (146), omitting the term  $T_{\text{ev}}/T_{\text{gas}}$ .

### 7.6 Davis-Greenstein torque

From equation (122), and the last sentence in Section 6.5, we take the dimensionless Davis-Greenstein torque to be

$$\langle \mathbf{\Gamma}'_{\text{DG}} \rangle = -\frac{\tau_{\text{drag}}}{\tau_{\text{DG}}} \left[ 1 + (r_2 - 1) \langle \sin^2 \gamma \rangle \right] \left( J'_{x,B} \hat{\mathbf{x}}_B + J'_{y,B} \hat{\mathbf{y}}_B \right). \quad (150)$$

It is somewhat more efficient to compute  $d\mathbf{J}$  due to the Davis-Greenstein torque in alignment coordinates rather than in angular-momentum coordinates.

### 7.7 Omission of the Barnett torque

The term  $J'_{x,B} \hat{\mathbf{x}}_B + J'_{y,B} \hat{\mathbf{y}}_B$  in equation (150) can also be expressed as  $J' \sin \xi (\hat{\boldsymbol{\xi}} \cos \xi + \hat{\mathbf{J}} \sin \xi)$ . As seen in equations (144)–(149) and the preceding sentence, none of the torques or diffusion coefficients considered so far depend explicitly on the coordinate  $\phi_B$ . The Barnett torque, due to the interaction of the grain's Barnett magnetic moment with the interstellar magnetic field, yields a rapid precession of the grain angular momentum about the field direction, i.e. rapid change of  $\phi_B$ . Since none of the processes here depend on  $\phi_B$ , for simplicity we omit the Barnett torque and set  $\phi_B = 0$  at the end of each time step.

### 7.8 Rotational averages

As described in Section 6 and seen in equations (144)–(150), several rotational averages involving the Eulerian angles (e.g.  $\langle \cos^2 \gamma \rangle$ ) are needed. As derived in Section 5, these are expressed in terms of  $\langle \text{dn}^2(\nu, k^2) \rangle$ ,  $\langle \text{cn}^2(\nu, k^2) \rangle$ , and  $\pi/[2K(k^2)]$ . We tabulate each of these quantities for  $10^4$  values of  $k^2$  between 0 and 0.9999 and interpolate. When  $k^2 > 0.9999$ , we employ the approximations

$$\langle \text{dn}^2(\nu, k^2) \rangle \approx \left[ \ln \left( \frac{4}{\sqrt{1-k^2}} \right) \right]^{-1} \quad (151)$$

and

$$K(k^2) \approx \left( 1 + \frac{1-k^2}{4} \right) \ln \left( \frac{4}{\sqrt{1-k^2}} \right) - \frac{1-k^2}{4}; \quad (152)$$

$\langle \text{cn}^2(\nu, k^2) \rangle$  is obtained from identity (55).

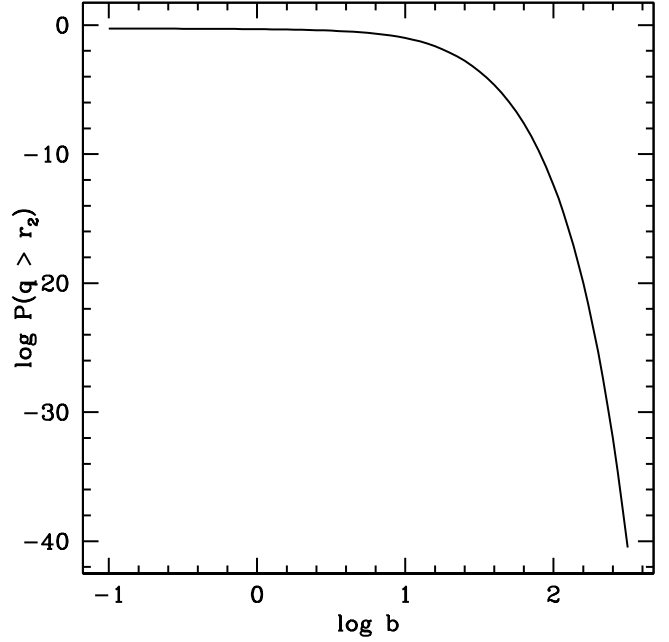


**Figure 2.** The probability that  $q > r_2$  for a thermal distribution, as a function of  $b$ .

### 7.9 Thermal averages over $q$

For sufficiently low  $J'$ ,  $q$  can reach values higher than  $r_2$  and flipping can occur. Of course, it is necessary to follow the evolution of  $q$  in this case. For high  $J'$ , the flipping probability is negligible, so it is sufficient to average the torque and diffusion coefficients, assuming a thermal distribution of  $q$  values. Fig. 2 shows the probability that  $q > r_2$  for a thermal distribution, as a function of  $b$ . We follow the evolution of  $q$  when  $b < b_{\text{crit}} = 300$  and average over  $q$  when  $b > b_{\text{crit}}$ , using equation (63) in Kolasi & Weingartner (2017) for the thermal-equilibrium distribution of  $q$ . Interpolation tables for thermally averaged quantities were generated using MATHEMATICA. Whenever  $b$  crosses  $b_{\text{crit}}$  from above, a value of  $q$  is randomly chosen from its thermal-equilibrium distribution for  $b = b_{\text{crit}}$ .

### 7.10 Time step size

In the high- $b$  regime, for which we average over  $q$ , we take a constant time step size  $dt' = k_{\text{high}}$ . In the low- $b$  regime, we take the step size  $dt' = k_{\text{low}} \tau'_{\text{int}}$ . In most simulations, we take  $k_{\text{low}} = 10^{-2}$  and  $k_{\text{high}} = 10^{-4}$ .

### 7.11 Grain flipping

When  $q < r_2$  ( $q > r_2$ ), the grain is in either the positive or negative flip state with respect to  $\hat{\mathbf{a}}_1$  ( $\hat{\mathbf{a}}_3$ ). Whenever  $q = r_2$  is crossed, the flip state is chosen randomly, with equal probability to be positive or negative. A grain flips when it starts with  $q < r_2$  in one flip state with respect to  $\hat{\mathbf{a}}_1$ , makes an excursion to  $q > r_2$ , and returns to  $q < r_2$  in the opposite flip state with respect to  $\hat{\mathbf{a}}_1$ .

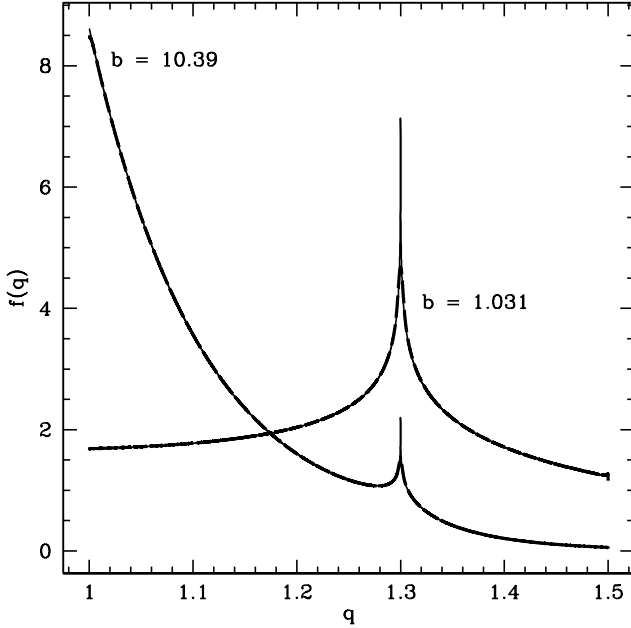


**Figure 3.** The thermal-equilibrium distribution function  $f(q)$  from simulations (heavy dashed curves) and theory (light solid curves) for two values of  $b$ , as indicated.

## 8 CODE TEST: THERMAL EQUILIBRIUM

In order to test both the theoretical development in Section 6 and our simulation code, we performed simulations with two simplified codes adopting thermal equilibrium.

### 8.1 Distribution of $q$

In the first code, external processes are omitted; the angular momentum and grain temperature are held constant and  $q$  is evolved using equation (128). In these simulations, the time step is taken to be  $10^{-3} \tau_{\text{int}}$  and the total duration of the simulation is  $10^8 \tau_{\text{int}}$ . The code returns the distribution function  $f(q)$ ; the fraction of the time that the grain has dimensionless energy parameter between  $q$  and  $q + dq$  is  $f(q)dq$ . These are compared with the theoretical distribution  $f_{\text{TE}}(q)$ , given by equation (63) in Kolasi & Weingartner (2017). Fig. 3 shows results from the simulations (heavy dashed curves) and theory (light solid curves) for two values of  $b$  (defined in eq. 131),  $b = 1.031$  and  $b = 10.39$ . There is a vertical asymptote at  $q = r_2 = 1.3$ , which the analytic equation better captures (with a finite number of values of  $q$  for which  $f_{\text{TE}}$  is evaluated) than the simulation. Otherwise, apart from slight deviations at  $q = 1$  and  $q = r_3$ , the results are identical.

### 8.2 Distribution of $J'$

In the second test, we check that the simulation correctly reproduces the distribution  $f(J')$ , defined such that the fraction of the time that the grain has dimensionless angular momentum between  $J'$  and  $J' + dJ'$  equals  $f(J') dJ'$ , in thermal equilibrium.

#### 8.2.1 Simulation

In this code, the only external processes are collisions and thermal evaporation. Thus, the mean torque and diffusion coefficients are given by equations (144)–(146), with  $T_{\text{ev}} = T_{\text{gas}} = T_d$ . The actual value of the temperature does not matter, since we are examining the distribution of  $J'$  rather than the distribution of  $J$ . In order to obtain results in a reasonable run time, we average all quantities over a thermal distribution of  $q$ , for all values of  $b$ . We take the time step and duration of the simulation equal to  $10^{-5} \tau_{\text{drag}}$  and  $10^5 \tau_{\text{drag}}$ , respectively. Table 1 indicates the adopted parameter values.

#### 8.2.2 Theoretical distribution function

For a freely rotating body, the Lagrangian  $L$  equals the rotational kinetic energy  $E$ ,

$$L = E = \frac{1}{2} I_1 \omega_1^2 + \frac{1}{2} I_2 \omega_2^2 + \frac{1}{2} I_3 \omega_3^2 \quad (153)$$

and the square of the angular momentum is

$$J^2 = I_1^2 \omega_1^2 + I_2^2 \omega_2^2 + I_3^2 \omega_3^2. \quad (154)$$

The components of the angular velocity along the principal axes can be expressed in terms of the Eulerian angles:

$$\omega_1 = \dot{\zeta} \cos \gamma + \dot{\alpha}, \quad (155)$$

$$\omega_2 = \dot{\zeta} \sin \alpha \sin \gamma + \dot{\gamma} \cos \alpha, \quad (156)$$

$$\omega_3 = \dot{\zeta} \cos \alpha \sin \gamma - \dot{\gamma} \sin \alpha, \quad (157)$$

where dots denote time derivatives. Inserting these into equation (153) for the Lagrangian, the momenta conjugate to the Eulerian angles are easily obtained; e.g.  $p_\zeta = \partial L / \partial \dot{\zeta}$ . After some algebra, we find  $E$  and  $J$  in terms of the Eulerian angles and their conjugate momenta, yielding

$$J' = \left\{ (p'_\alpha)^2 + \left[ \cos \alpha p'_\gamma + \frac{\sin \alpha}{\sin \gamma} (p'_\zeta - \cos \gamma p'_\alpha) \right]^2 + \left[ \sin \alpha p'_\gamma - \frac{\cos \alpha}{\sin \gamma} (p'_\zeta - \cos \gamma p'_\alpha) \right]^2 \right\}^{1/2}, \quad (158)$$

$$q = (J')^{-2} \left\{ (p'_\alpha)^2 + r_2 \left[ \cos \alpha p'_\gamma + \frac{\sin \alpha}{\sin \gamma} (p'_\zeta - \cos \gamma p'_\alpha) \right]^2 + r_3 \left[ \sin \alpha p'_\gamma - \frac{\cos \alpha}{\sin \gamma} (p'_\zeta - \cos \gamma p'_\alpha) \right]^2 \right\}, \quad (159)$$

where  $p'_i = p_i / (I_i \omega_T)$ .

The grain rotational states are uniformly distributed in the 6-dimensional phase space defined by the Eulerian angles and their conjugate momenta, but neither  $J'$  nor  $q$  depends explicitly on  $\zeta$ . Define the density of states  $\rho(J', q)$  such that the number of states with dimensionless angular momentum and rotational energy between  $J'$  and  $J' + dJ'$  and  $q$  and  $q + dq$  is proportional to  $\rho(J', q) dJ' dq$ . To estimate the density of states, we calculate  $J'$  and  $q$  for (230)<sup>5</sup> combinations of  $(\gamma, \alpha, p'_\zeta, p'_\gamma, p'_\alpha)$ , with the angles uniformly distributed from 0 to  $2\pi$  and the conjugate momenta distributed logarithmically from  $7 \times 10^{-4}$  to 3. We have tried other values for the number of combinations and range of values of the

**Table 1.** Adopted parameter values for simulations.

symbol	quantity	section 8.2.1 thermal equil	section 10 f-step bias	section 11 crossovers suite 1	section 12 D-G case 1
$\delta$	spheroid semilength ratio	0.5	0.5	0.5	0.5
$r_2$	$I_1/I_2$	1.3	1.3	1.3	1.3
$r_3$	$I_1/I_3$	1.5	1.5	1.5	1.5
$\bar{\rho}$	grain mean density ( $\text{g cm}^{-3}$ )	3.0	3.0	3.0	3.0
$n_{\text{H}}$	gas H number density ( $\text{cm}^{-3}$ )	30	30	30	30
$a_{\text{eff}}$	grain effective radius ( $\mu\text{m}$ )	0.2	0.2	0.2	0.2
$T_{\text{gas}}$	gas temperature (K)	NA	100	100	100
$T_d$	dust temperature (K)	NA	15	15	15
$N_s$	number of $\text{H}_2$ -formation sites	NA	$5.5 \times 10^5$	$5.5 \times 10^5$	$5.5 \times 10^5$
$E_{\text{H}_2}$	$\text{H}_2$ kinetic energy (eV)	NA	0.2	0.2	0.2
$(\cos \theta_{\text{out}})_{\text{min}}$	see Section 9	NA	0.8	0.8	0.8
$B$	interstellar magnetic field ( $\mu\text{G}$ )	NA	NA	NA	5.0
$t'_{\text{life}}$	$\text{H}_2$ -formation site lifetime	NA	NA	NA	1
$k_{\text{low}}$	low- $b$ time-step parameter	NA	$10^{-2}$	$10^{-2}$	$10^{-2}$
$k_{\text{high}}$	high- $b$ time-step parameter	$10^{-5}$	NA	$10^{-4}$	$10^{-4}$
$t'$	duration of simulation (if fixed)	$10^5$	NA	NA	$10^3$

momenta and found that the distribution function for the relevant range of  $J'$  and  $q$  is well converged.

The thermal-equilibrium distribution of  $J'$  is

$$f(J') = \int_1^{r_3} dq \rho(J', q) \exp\left[-\frac{\alpha_1}{2} (J')^2\right]; \quad (160)$$

the form of the Boltzmann factor follows from equations (1), (20), and (126). The temperature does not explicitly appear because the variable is  $J'$  rather than  $J$ .

### 8.2.3 Results

Fig. 4 shows the results from both simulation and theory, which agree perfectly.

## 9 $\text{H}_2$ FORMATION

In the following sections, we will assume that all H atoms depart the grain surface within  $\text{H}_2$  molecules, formed at special surface sites.

Draine & Weingartner (1997) took the surface area per  $\text{H}_2$ -formation site equal to  $l^2$ , with  $l^2 = 100 \text{ \AA}^2$  as a fiducial value. They also considered larger values of  $l^2$ . The surface area of an oblate spheroid is

$$S = 2\pi a_{\text{eff}}^2 \delta^{-2/3} \left[1 + \delta^2 g(\delta)\right]. \quad (161)$$

For  $a_{\text{eff}} = 0.2 \mu\text{m}$  and  $\delta = 0.5$ ,  $S = 5.5 \times 10^7 \text{ \AA}^2$ . Thus, for  $l^2 = 100 \text{ \AA}^2$ , the number of  $\text{H}_2$ -formation sites is  $N_s = 5.5 \times 10^5$ . We will adopt this value in our simulations.

The translational kinetic energy of the ejected  $\text{H}_2$  molecule is not well known. In most simulations, we take  $E_{\text{H}_2} = 0.2 \text{ eV}$ , but we also perform some simulations with  $E_{\text{H}_2} = 0.05 \text{ eV}$  and  $1.0 \text{ eV}$ .

At the start of each simulation, the locations of all  $N_s$  sites, as well as the departure directions at the sites, are chosen randomly as described in Section 6.4.2, taking  $(\cos \theta_{\text{out}})_{\text{min}} = 0.8$ . To provide a sense for the magnitude of the dimensionless efficiency factors  $Q_i$  ( $i = 1-8$ ) defined in Section 6.4.2, Table 2 tabulates their values for one particular grain realization with  $N_s = 5.5 \times 10^5$ .

If a grain reaches suprathermal rotation, then  $q \approx 1$  and  $\gamma \approx 0$ . Setting the systematic and drag torques (equations 147 and 148)

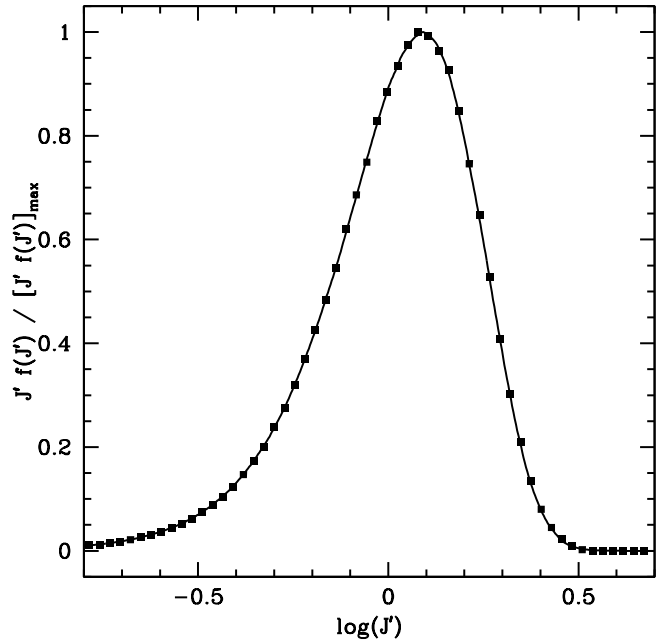


**Figure 4.**  $J' f(J')$ , normalized to its maximum value, for thermal equilibrium. The solid curve is for the simulation results and the boxes are the theoretical result.

**Table 2.** Efficiency factors associated with  $\text{H}_2$  formation for one grain realization with number of special sites  $N_s = 5.5 \times 10^5$ .

$Q_1$	$-4.00 \times 10^{-4}$
$Q_2$	$3.13 \times 10^{-4}$
$Q_3$	0.600
$Q_4$	0.521
$Q_5$	0.599
$Q_6$	$9.04 \times 10^{-2}$
$Q_7$	$9.01 \times 10^{-2}$
$Q_8$	$5.40 \times 10^{-2}$

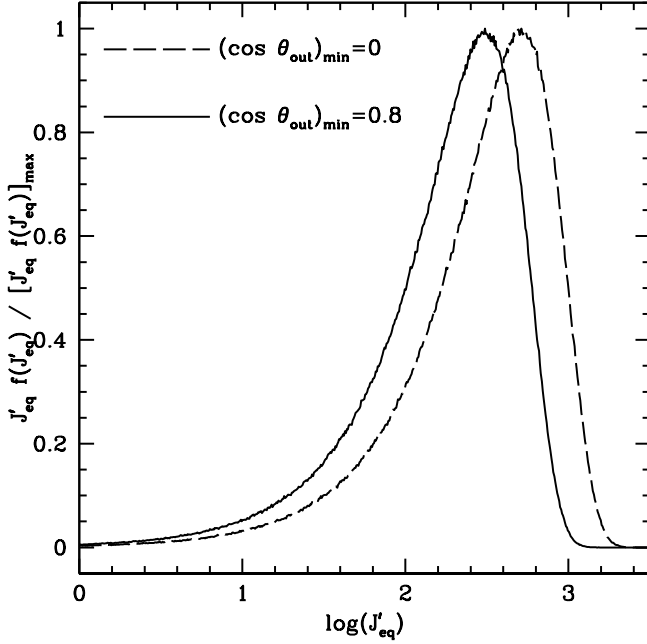


**Figure 5.** Distribution of  $J'_{\text{eq}}$  for randomly constructed grain realizations with  $(\cos \theta_{\text{out}})_{\text{min}} = 0$  or  $0.8$  (see text). Parameters are as in Table 1, with  $E_{\text{H}_2} = 0.2$  eV, and  $N_s = 5.5 \times 10^5$ . The distribution function  $f(J'_{\text{eq}})$  is defined such that the fraction of grain with dimensionless equilibrium angular momentum between  $J'_{\text{eq}}$  and  $J'_{\text{eq}} + dJ'_{\text{eq}}$  equals  $f(J'_{\text{eq}}) dJ'_{\text{eq}}$ .

equal yields the equilibrium value of the dimensionless angular momentum:

$$J'_{\text{eq}} = \frac{\delta^{1/3} Q_1 v_{\text{H}_2}}{Q_3 a_{\text{eff}} \omega_T}. \quad (162)$$

In this expression, a positive (negative) value corresponds to rotation with positive (negative) flip state with respect to  $\hat{a}_1$ . Given the relevant parameters in Table 1 and the efficiency factors in Table 2,  $J'_{\text{eq}} = 395$ . In equilibrium, this grain is in the negative flip state with respect to  $\hat{a}_1$ .

Fig. 5 shows the distribution of  $J'_{\text{eq}}$  derived from  $6.4 \times 10^6$  different grain realizations randomly constructed as described in Section 6.4.2, with the relevant parameters as in Table 1, except for  $(\cos \theta_{\text{out}})_{\text{min}}$  equal to both 0 and 0.8.

From equations (78), (79), (113), and (119)–(121), in the limit of uniform surface coverage of formation sites with  $(\cos \theta_{\text{out}})_{\text{min}} = 0$ ,  $Q_6$  and  $Q_7 \rightarrow Q_{6,\text{un}}$  and  $Q_8 \rightarrow Q_{8,\text{un}}$ , where

$$Q_{6,\text{un}} = \frac{Z_2(\delta)}{3[1 + \delta^2 g(\delta)]}, \quad (163)$$

$$Q_{8,\text{un}} = \frac{Z_1(\delta)}{3[1 + \delta^2 g(\delta)]}. \quad (164)$$

Recall that the functions  $Z_1(\delta)$  and  $Z_2(\delta)$  are defined in equations (80) and (81). For  $\delta = 0.5$ ,  $Q_{6,\text{un}} = 0.1187$  and  $Q_{8,\text{un}} = 0.1501$ . In our suite of  $6.4 \times 10^6$  different grain realizations with  $(\cos \theta_{\text{out}})_{\text{min}} = 0$ ,  $Q_6$  and  $Q_7$  are always within 1% of  $Q_{6,\text{un}}$  and  $Q_8$  is always within 1% of  $Q_{8,\text{un}}$ . For the suite with  $(\cos \theta_{\text{out}})_{\text{min}} = 0.8$ ,  $Q_6$  and  $Q_7$  are always close to  $0.76 Q_{6,\text{un}}$  and  $Q_8$  is always close to  $0.36 Q_{8,\text{un}}$ .

In Section 11, where we examine the duration of and disalignment during a single crossover, the efficiency factors  $Q_1$ – $Q_8$

associated with  $\text{H}_2$  formation are held fixed throughout the simulation. In Section 12, examining Davis-Greenstein alignment, existing formation sites are destroyed and new formation sites are formed, so that  $Q_1$ – $Q_8$  vary throughout the simulation. For simplicity, and to keep the total number of special formation sites,  $N_s$ , constant, we assume that when a site is destroyed, another site forms at the same time. The probability that no sites are destroyed during time  $\Delta t_{\text{rep}}$  is given by

$$P_{\text{none}} = \exp\left(-\frac{N_s \Delta t_{\text{rep}}}{t_{\text{life}}}\right), \quad (165)$$

where  $t_{\text{life}}$  is the site lifetime. Thus, we take the time until the next site-replacement event to be

$$\Delta t_{\text{rep}} = -\frac{t_{\text{life}} \ln P}{N_s}, \quad (166)$$

where  $P$  is a random number between 0 and 1. During a site-replacement event, one existing site is randomly chosen for destruction. A new site is immediately formed, with parameters chosen randomly following the same prescription for constructing the sites at the start of the simulation. We perform simulations with three values of  $t'_{\text{life}} = t_{\text{life}}/\tau_{\text{drag}} = 1, 10, \text{ and } 10^3$ .

## 10 F-STEP DURATION BIAS

In this section, we present an example to illustrate the  $f$ -step duration bias described in Section 1. Recall that we define an  $f$ -step as the interval between consecutive flips and define up-steps and down-steps as  $f$ -steps with  $\mathbf{J} \cdot \Gamma_1 \hat{a}_1 > 0$  and  $\mathbf{J} \cdot \Gamma_1 \hat{a}_1 < 0$ , respectively. In an up-step, the systematic torque acts so as to spin the grain up to higher angular momentum; the opposite applies in a down-step.

We ran four suites of simulations, with parameter values as given in Table 1. The special sites are held fixed and are identical for all of the simulations. The values of the efficiency factors associated with  $\text{H}_2$  formation are given in Table 2. The Davis-Greenstein torque is not included. The time step parameter  $k_{\text{low}} = 10^{-2}$ ;  $k_{\text{high}}$  is not relevant, since the high- $b$  regime never applies.

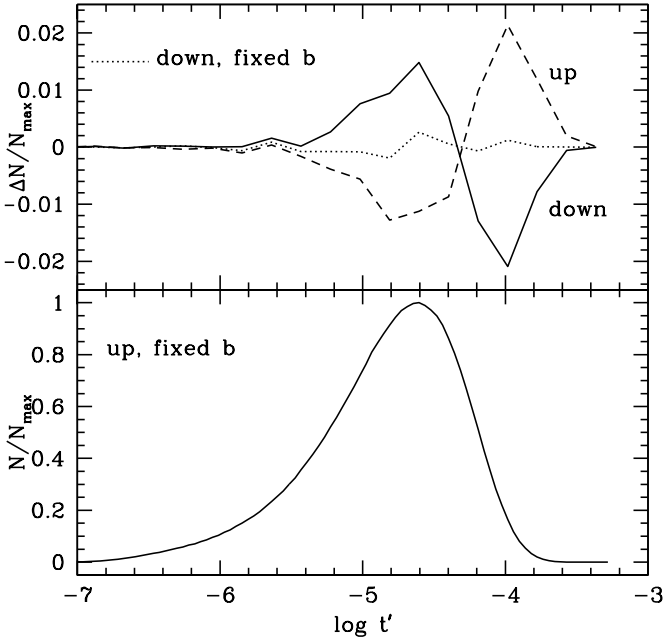
Each suite consists of  $4 \times 10^6$  simulations and each simulation starts with  $J' = 2$  and  $q = 1.01$ . Each simulation is terminated when the flip state with respect to  $\hat{a}_1$  changes. Thus, each simulation corresponds approximately to one  $f$ -step. Note that Kolasi & Weingartner (2017) adopted a more realistic, but also more complicated, definition of a flip; the simple approximation here is sufficient for our purpose. Suites 1 and 2 are for an up-step and a down-step, respectively. Likewise for suites 3 and 4, except that the parameter  $b$ , which depends on  $J'$  and is defined in equation (131), is held fixed throughout the simulation in these cases. To be clear, the value of  $J'$  changes in all of the simulations, but in suites 3 and 4, we do not adjust the value of  $b$  accordingly. Only the internal relaxation is affected by the value of  $b$ ; by holding it constant, we artificially eliminate the dependence of the flipping probability per unit time on  $J'$ .

Table 3 shows the mean value of the (dimensionless)  $f$ -step duration,  $t'_{\text{av}}$ , and the mean value of the change in the (dimensionless) angular momentum,  $(\Delta J')_{\text{av}}$ , for each suite. Both  $t'_{\text{av}}$  and  $|(\Delta J')_{\text{av}}|$  are nearly identical for suites 3 and 4, as expected since the internal relaxation is taken to be independent of  $J'$  in these simulations. Also as expected, the values of  $t'_{\text{av}}$  and  $(\Delta J')_{\text{av}}$  are larger for suite 1 (up-steps) than for suites 3 and 4, and are both smaller for suite 2 (down-steps).

The bottom panel of Fig. 6 shows the histogram  $N/N_{\text{max}}$  of

**Table 3.** Mean f-step duration and change in angular momentum.

Suite	Description	$t'_{av}$	$(\Delta J')_{av}$
1	up-step	$2.54 \times 10^{-5}$	$5.78 \times 10^{-3}$
2	down-step	$2.39 \times 10^{-5}$	$-5.44 \times 10^{-3}$
3	up-step (fixed $b$ )	$2.46 \times 10^{-5}$	$5.59 \times 10^{-3}$
4	down-step (fixed $b$ )	$2.46 \times 10^{-5}$	$-5.60 \times 10^{-3}$

**Figure 6.** Bottom panel: Histogram  $N/N_{\max}$  of  $\log t'$  for suite 3 (up-steps, constant  $b$ ), normalized at its peak. Top panel: The difference  $\Delta N/N_{\max}$  between the histogram for suites 1 (up-steps, dashed), 2 (down-steps, solid), and 4 (down-steps, fixed  $b$ , dotted).

$\log t'$  for suite 3, normalized at its peak. The top panel shows the difference  $\Delta N/N_{\max}$  between the histogram for each of the other three suites and suite 3. The difference is relatively small for suite 4; it should approach zero as the number of simulations per suite increases. For suite 1 (up-steps), there is an excess at the longest times, compensated by a deficit at shorter times. The opposite trend applies for suite 2 (down-steps).

## 11 CROSSOVERS

In this section, we examine the duration of individual crossovers, as well as the disalignment during the crossover. Each simulation begins with the construction of the special sites, as described in Section 9. We demand that  $J'_{eq} \geq 50$ ; otherwise, the construction is discarded and a new one is generated. The initial dimensionless angular momentum is set equal to  $J'_c = (1 - e^{-1})J'_{eq} \approx 0.632 J'_{eq}$ . The flip state is chosen such that the systematic torque spins the grain down, to lower values of  $J'$ . During the simulation, the special sites are held fixed. The simulation ends when  $J' = J'_c$ , in the flip state such that the systematic torque is spinning the grain up.

These simulations include internal relaxation and only two external processes: collisions and  $H_2$  formation at special sites (sec-

tion 7.5). The Davis-Greenstein torque is not included. Initially, the grain is oriented such that the alignment angle  $\xi = 0$ . Thus, the value of  $\cos \xi$  at the end of the simulation indicates the disalignment:  $\cos \xi = 1$  implies no angular deviation of the angular momentum vector during the crossover.

Now suppose that the grain is constrained to always rotate about  $\hat{a}_1$  and is only subject to the mean systematic and drag torques. That is, stochastic elements are neglected. In this case, the grain spins down from  $J'_c$  to  $J' = 0$  and then back up to  $J'_c$ , without any flip and with the final angular momentum pointing in the opposite direction as the initial angular momentum. In this case, the duration  $t'_s$  of the crossover (normalized to the drag time) can be found analytically:

$$t'_s = \frac{4}{3[1 + \delta^2 g(\delta)]Q_3} \ln \left( \frac{1 + J'_c/J'_{eq}}{1 - J'_c/J'_{eq}} \right) \approx \frac{1.987}{[1 + \delta^2 g(\delta)]Q_3}. \quad (167)$$

If thermal trapping is important, then we would expect that  $t'/t'_s \gg 1$ , where  $t'$  is the actual duration of the crossover as found in the simulation.

We ran four suites of simulations. The parameter values for suite 1 are given in Table 1. Each suite consists of  $5.6 \times 10^4$  separate simulations with identical input parameter values; only the seed for the random number generator differs among the simulations within a suite. For suites 2 and 3, different values are adopted for the kinetic energy of the outgoing  $H_2$  molecules:  $E_{H_2} = 0.05$  eV and 1.0 eV. For suites 1–3, the step-size parameters (see Section 7.10) are taken to be  $k_{low} = 10^{-2}$  and  $k_{high} = 10^{-4}$ . Suite 4 serves as a convergence check, with  $E_{H_2} = 0.2$  eV,  $k_{low} = 10^{-3}$ , and  $k_{high} = 10^{-5}$ .

Figures 7–9 show the following three distribution functions for suites 1–3: (1)  $\cos \xi$ ; (2)  $t'/t'_s$ , the ratio of the crossover duration  $t'$  to the duration  $t'_s$  for the simple case described above; and (3)  $\log J'_{min}$ , where  $J'_{min}$  is the minimum value of  $J'$  during the crossover. In each case,  $f_i(u) du$  equals the fraction of simulations for which the argument lies between  $u$  and  $u + du$ . The three distribution functions are denoted by subscripts ‘ $\xi$ ’, ‘ $t$ ’, and ‘ $J$ ’, respectively, for  $\cos \xi$ ,  $t'/t'_s$ , and  $\log J'_{min}$ .

Generally, the disalignment is mild and the duration is comparable to  $t'_s$ . That is, thermal trapping is not a prevalent condition. The distribution functions display clear trends as a function of the  $H_2$  kinetic energy. As  $E_{H_2}$  increases, the distributions shift towards more disalignment, longer duration, and lower minimum value of  $J'$ . Table 4 shows the fraction of the simulations within each suite for which  $\cos \xi$  and  $J'_{min}$  are less than the lower limits in Figs. 7 and 9 and for which  $t'/t'_s$  is greater than the upper limit in Fig. 8. The tails of the distributions favor longer durations and lower  $J'_{min}$  for lower  $E_{H_2}$ , though the precision far out in the tails is, of course, low.

As noted above, simulation suites 1–3 take step-size parameters  $k_{low} = 10^{-2}$  and  $k_{high} = 10^{-4}$ . To check if these yield sufficient convergence, suite 4 repeats suite 1, except with  $k_{low} = 10^{-3}$  and  $k_{high} = 10^{-5}$ . We find that the distribution functions are virtually identical for these two suites. The largest discrepancy is for  $f_{\xi}(\cos \xi)$ . To illustrate the fine agreement even for this case, we examine the cumulative distribution function,  $f_{\xi,cum}(\cos \xi)$ , starting at  $\cos \xi = 1$ . That is,  $f_{\xi,cum}(\cos \xi) = \int_{\cos \xi}^1 f_{\xi}(u) du$ . Figure 10 shows  $\Delta(\cos \xi)$  versus  $\cos \xi$ , where  $\Delta(\cos \xi)$  is the fractional difference between the cumulative distribution function for the two suites.

As noted in Section 7.2, we adopt ‘reflecting’ boundary conditions at  $q = 1$  and  $q = r_3$ , since this choice best reproduces the distribution function for  $q$  in the case of thermal equilibrium. Otherwise, this choice is arbitrary. As a check on the extent to which



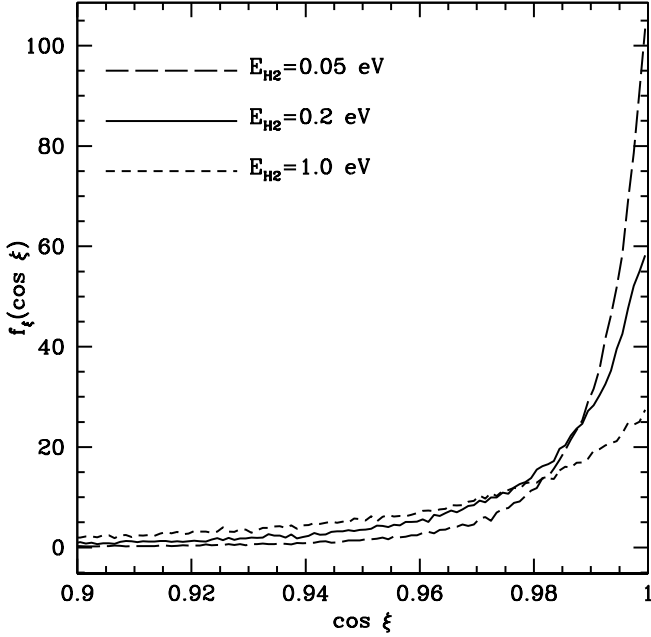


**Figure 7.** The distribution function  $f_{\xi}(\cos \xi)$  for suites of crossover simulations with the energy  $E_{\text{H}_2}$  of the departing  $\text{H}_2$  molecule as indicated. See the text for other parameter values.

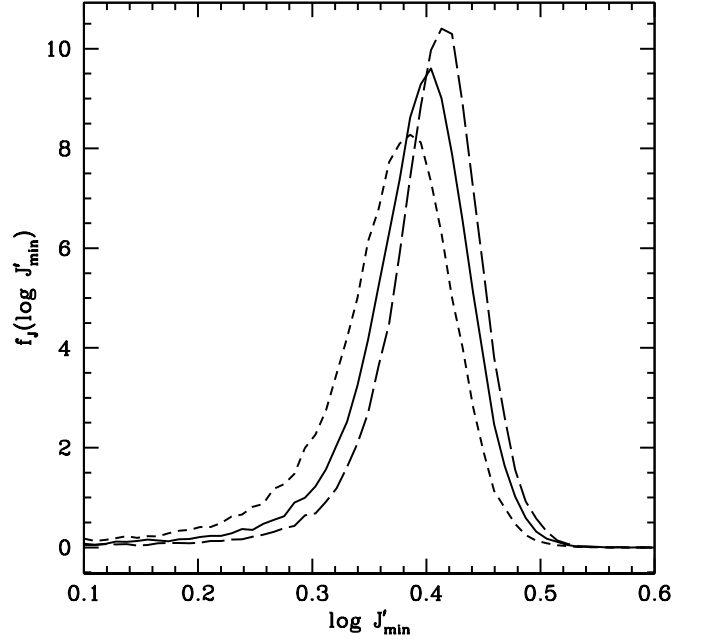


**Figure 9.** Same as Figure 7 except for the distribution function  $f_J(\log J'_{\min})$ . Line types as in Figure 7.

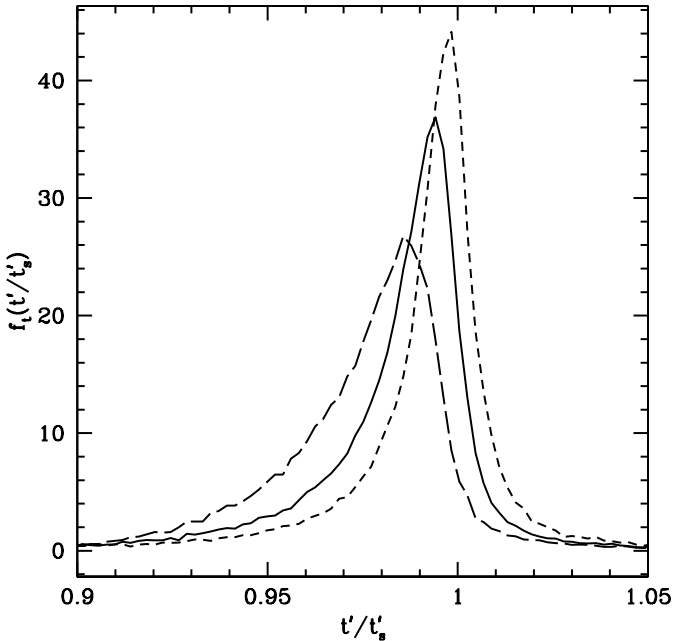


**Figure 8.** Same as Figure 7 except for the distribution function  $f_t(t'/t'_s)$ . Line types as in Figure 7.

**Table 4.** Fraction of the crossover simulations satisfying outlying conditions.

Condition	$E_{\text{H}_2} = 0.05 \text{ eV}$	$E_{\text{H}_2} = 0.2 \text{ eV}$	$E_{\text{H}_2} = 1.0 \text{ eV}$
$\cos \xi < 0.9$	$3.55 \times 10^{-2}$	$6.24 \times 10^{-2}$	0.195
$\cos \xi < 0.8$	$2.66 \times 10^{-2}$	$2.67 \times 10^{-2}$	$8.93 \times 10^{-2}$
$\cos \xi < 0.5$	$1.79 \times 10^{-2}$	$1.10 \times 10^{-2}$	$2.35 \times 10^{-2}$
$\cos \xi < 0$	$1.07 \times 10^{-2}$	$5.32 \times 10^{-3}$	$6.62 \times 10^{-3}$
$\cos \xi < -0.5$	$4.80 \times 10^{-3}$	$2.00 \times 10^{-3}$	$2.43 \times 10^{-3}$
$t'/t'_s > 1.05$	$4.91 \times 10^{-2}$	$3.30 \times 10^{-2}$	$1.78 \times 10^{-2}$
$t'/t'_s > 2.0$	$1.98 \times 10^{-2}$	$7.68 \times 10^{-4}$	0
$t'/t'_s > 3.0$	$1.24 \times 10^{-2}$	$5.36 \times 10^{-5}$	0
$t'/t'_s > 4.0$	$7.73 \times 10^{-3}$	$1.79 \times 10^{-5}$	0
$t'/t'_s > 10.0$	$9.82 \times 10^{-4}$	0	0
$J'_{\min} < 10^{-1}$	$9.88 \times 10^{-3}$	$2.05 \times 10^{-3}$	$1.34 \times 10^{-3}$
$J'_{\min} < 3 \times 10^{-2}$	$5.07 \times 10^{-3}$	$9.29 \times 10^{-4}$	$5.89 \times 10^{-4}$
$J'_{\min} < 10^{-2}$	$3.11 \times 10^{-3}$	$5.00 \times 10^{-4}$	$2.86 \times 10^{-4}$
$J'_{\min} < 3 \times 10^{-3}$	$1.89 \times 10^{-3}$	$2.32 \times 10^{-4}$	$7.14 \times 10^{-5}$
$J'_{\min} < 10^{-3}$	$7.14 \times 10^{-4}$	$3.57 \times 10^{-5}$	0

this choice affects the results, we repeated all four simulation suites with a different prescription for the boundaries. In these runs, if a time step yields  $q < 1$  or  $q > r_3$ , then a new value of  $d\omega'_{\text{int}}$  is selected randomly and  $dq$  is recomputed. The distribution functions resulting from suites with the two different boundary prescriptions differ very slightly.

## 12 DAVIS-GREENSTEIN ALIGNMENT

In this section, we examine the efficiency of Davis-Greenstein alignment. We constructed seven suites of simulations which include internal relaxation, collisions with gas atoms,  $\text{H}_2$  formation at time-varying special sites (Section 9), and the Davis-Greenstein torque.

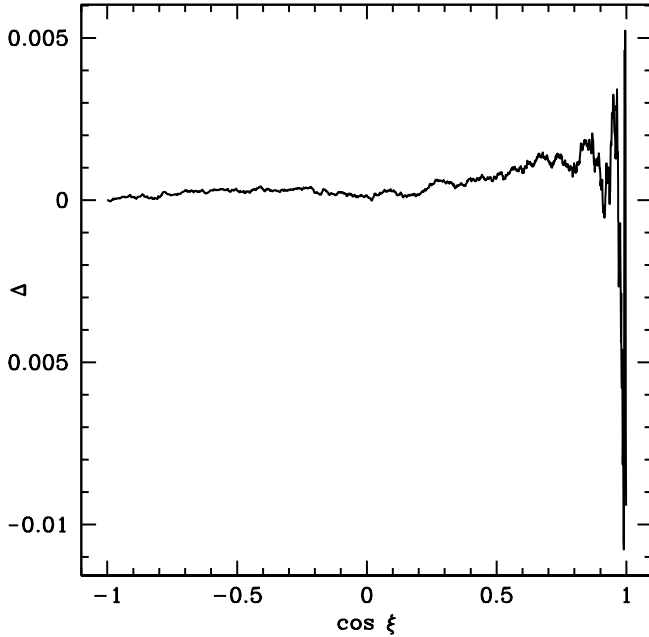


**Figure 10.** The fractional difference  $\Delta(\cos \xi)$  between the cumulative distribution function (starting at  $\cos \xi = 1$ ) for two simulation suites with  $E_{\text{H}_2} = 0.2$  eV. The time-step parameters for the two suites are  $(k_{\text{low}}, k_{\text{high}}) = (10^{-2}, 10^{-4})$  and  $(10^{-3}, 10^{-5})$ .

Each suite consists of 504 simulations. At the start of each simulation, the grain is randomly constructed as in previous sections, the alignment angle  $\xi$  is randomly chosen from a uniform distribution in  $\cos \xi$  (with  $-1 \leq \cos \xi \leq 1$ ), and  $J'$  is set equal to 2.5, which corresponds to the peak of the distribution  $f_J(\log J'_{\text{min}})$  for the suite of crossover simulations with  $E_{\text{H}_2} = 0.2$  eV (Fig. 9).

For our reference suite ('case 1'), we take parameter values as in Table 1; the total duration of the simulation (normalized to the drag time-scale)  $t' = 10^3$ . For each of the other suites, one or more of the parameter values are changed, as indicated in Table 5. In cases 2 and 3, the site lifetime is increased. In case 4, thermal trapping is artificially prohibited, in the following extreme manner: Each time the low- $b$  regime is entered, after the first  $q = r_2$  crossing, the flip state (with respect to both  $\hat{a}_1$  and  $\hat{a}_3$ ) is always chosen such as to spin the grain up. Case 5 is a convergence check, with the two parameters  $k_{\text{low}}$  and  $k_{\text{high}}$  both reduced by an order of magnitude; the duration  $t'$  of the simulation is also reduced by an order of magnitude to avoid unmanageable run times. In case 6, the dust temperature is increased to  $T_d = 20$  K. Finally, in case 7, a smaller grain size,  $a_{\text{eff}} = 0.05 \mu\text{m}$ , is considered. In this case, the number of special sites  $N_s$  is reduced in proportion to the grain surface area (i.e. by a factor of 16). Since the internal relaxation time  $\tau_{\text{int}}$  decreases for the smaller grain, the duration of the simulation is also decreased, to 100 drag times, to avoid unmanageable run times.

As an illustration of the grain dynamics, Figs. 11 and 12 show  $J'_{\text{eq}}$ ,  $\log J'$ , and  $\cos \xi$  versus  $t'$  for one of the 504 Davis-Greenstein simulations, for cases 1 and 2, respectively. These cases differ only in that  $t'_{\text{life}} = 1$  for case 1 and  $10^3$  for case 2. Consequently,  $J'_{\text{eq}}$  and  $J'$  fluctuate much more rapidly for case 1 than for case 2. The plots are generated using  $10^3$  output times (one per drag time); the fluctuations of  $J'_{\text{eq}}$  and  $J'$  are actually more pronounced than

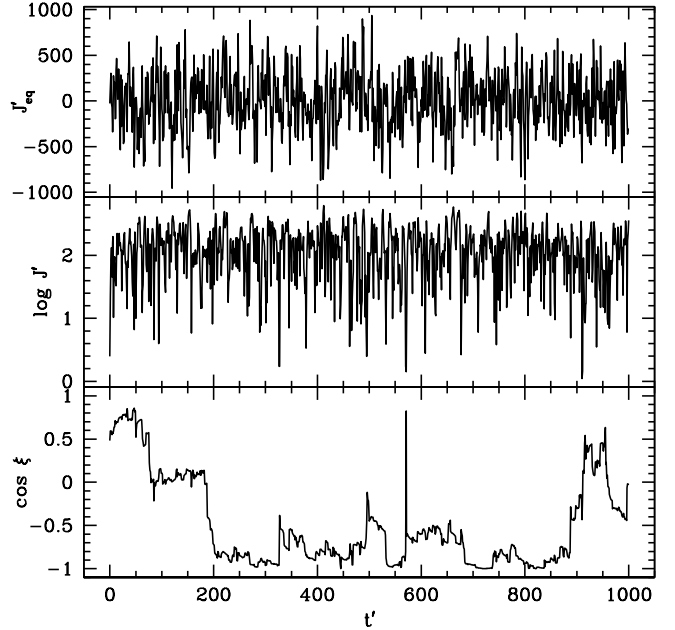


**Figure 11.**  $J'_{\text{eq}}$ ,  $\log J'$ , and  $\cos \xi$  versus  $t'$  for one of the 504 case-1 Davis-Greenstein simulations.

indicated in the figure, as would be seen if more output times were used in the figure construction.

The Rayleigh reduction factor,

$$\text{RRF} = \frac{3}{2} \left( \cos^2 \xi - \frac{1}{3} \right), \quad (168)$$

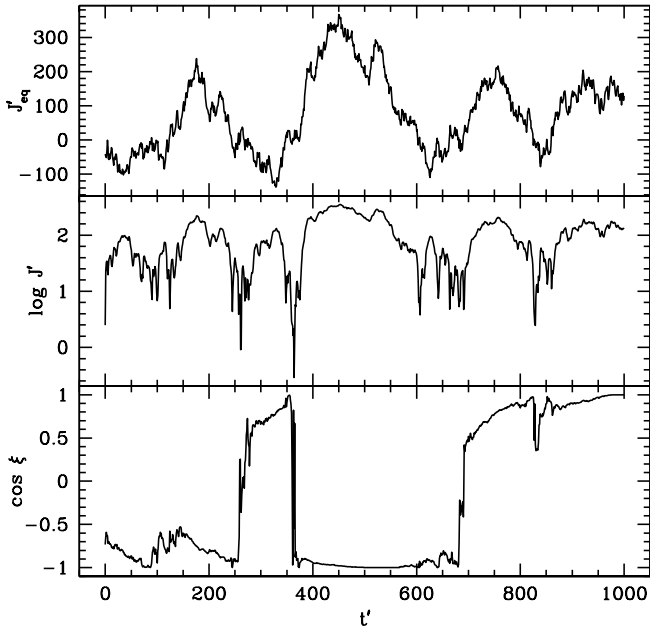
is a useful measure of the grain alignment efficiency. In the Rayleigh limit, the linear dichroism of a grain rotating about  $\hat{a}_1$  is proportional to RRF (Lee & Draine 1985). For alignment, RRF must exceed zero; larger values of RRF correspond to higher degrees of alignment.

Fig. 13 shows  $\text{RRF}_{\text{av}}(10)$ ,  $\text{RRF}_{\text{av}}(10^2)$ , and  $\text{RRF}_{\text{av}}(10^3)$  versus  $\cos \xi_0$  for case 1, where  $\text{RRF}_{\text{av}}(t')$  is the time-averaged Rayleigh reduction factor, from the start of the simulation to dimensionless time  $t' = t/\tau_{\text{drag}}$ , and  $\xi_0$  is the initial value of  $\xi$ . That is, the time average is taken over the first 10 drag times, the first  $10^2$  drag times, and the entire simulation (with duration  $10^3$  drag times). Each point represents one of the 504 simulations. For the adopted parameters,  $\tau_{\text{DG}}/\tau_{\text{drag}} = 73.3$ . That is, the alignment time-scale equals 73.3 times the drag time-scale. Thus, the plot of  $\text{RRF}_{\text{av}}(t')$  versus  $\cos \xi_0$  resembles that of equation (168) for early  $t'$ . By  $t' = 10^3$ , the time-averaged Rayleigh reduction factor no longer shows a dependence on the initial value of the alignment angle  $\xi_0$  and is positive for most simulations.

For each of the seven simulation suites, table 5 provides the values of  $\langle \text{RRF}_{\text{av}}(t') \rangle$ , the average of  $\text{RRF}_{\text{av}}(t')$  over all 504 simulations (with  $t' = 10, 10^2$ , and  $10^3$ , where applicable). On times  $\sim 10^2$ – $10^3 \tau_{\text{drag}}$ , paramagnetic dissipation does yield partial grain alignment. As expected, the alignment is more efficient for larger values of the  $\text{H}_2$ -formation site lifetime (cases 1–3). Thermal trapping does not prevent D-G alignment, though the alignment may be somewhat more efficient in case 4, where thermal trapping is artificially prohibited in an extreme manner. Comparing the results for cases 1 and 5, we conclude that the adopted values for the time-step

**Table 5.** Cases for Davis-Greenstein simulations.

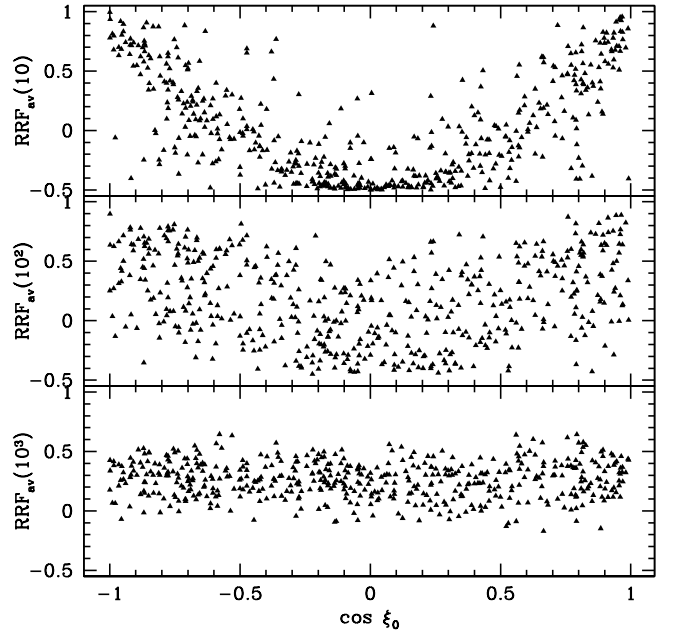
Case	Difference from Case 1	$\langle \text{RRF}_{\text{av}}(10) \rangle$	$\langle \text{RRF}_{\text{av}}(10^2) \rangle$	$\langle \text{RRF}_{\text{av}}(10^3) \rangle$
1	NA	0.038	0.187	0.265
2	$t'_{\text{life}} = 10^3$	0.046	0.269	0.698
3	$t'_{\text{life}} = 10$	0.014	0.190	0.413
4	prohibited thermal trapping (see text)	0.028	0.201	0.413
5	$k_{\text{low}} = 10^{-3}$ , $k_{\text{high}} = 10^{-5}$ , $t' = 10^2$	0.039	0.152	NA
6	$T_d = 20$ K	0.049	0.131	0.214
7	$a_{\text{eff}} = 0.05 \mu\text{m}$ ; $N_s = 34, 400$ ; $t' = 10^2$	0.094	0.412	NA


**Figure 12.**  $J'_{\text{eq}}$ ,  $\log J'$ , and  $\cos \xi$  versus  $t'$  for one of the 504 case-2 Davis-Greenstein simulations.

parameters  $k_{\text{low}}$  and  $k_{\text{high}}$  are reasonable. That is, the simulations appear to be well converged.

For all except case 7, the grain size  $a_{\text{eff}} = 0.2 \mu\text{m}$ , for which (given the adopted CNM-like parameter values)  $\tau_{\text{drag}} = 1.3 \times 10^5$  yr and  $\tau_{\text{DG}}/\tau_{\text{drag}} = 73$ . Thus, times  $\sim 10^2$ – $10^3 \tau_{\text{drag}}$  equate to 13–130 Myr. From simulations of the multiphase interstellar medium, Peters et al. (2017) find a broad distribution of dust residence times in the CNM, with a median around 7 Myr. Thus, the time required for D-G alignment of grains with  $a_{\text{eff}} = 0.2 \mu\text{m}$  seems uncomfortably long.

Furthermore,  $\tau_{\text{drag}} \propto a_{\text{eff}}$  and  $\tau_{\text{DG}} \propto a_{\text{eff}}^2$  (eqs. 127 and 123). Thus, for  $a_{\text{eff}} = 0.05 \mu\text{m}$ ,  $\tau_{\text{drag}} = 3.3 \times 10^4$  yr and  $\tau_{\text{DG}}/\tau_{\text{drag}} = 18$ . As seen from the case-7 result, moderately efficient alignment is achieved on a time  $\sim 10^2 \tau_{\text{drag}} \sim 3.3$  Myr. Thus, D-G alignment in the CNM is more plausible for relatively small grains than for relatively large grains, whereas observations reveal that only the relatively large grains are well aligned (Kim & Martin 1995). This contradiction between the model and observations has long plagued the D-G theory, even prior to the modifications by Purcell. In their original work on thermal trapping, considering only Barnett relaxation, Lazarian & Draine (1999a) found thermal trap-


**Figure 13.** The Rayleigh reduction factor time-averaged over the first 10 drag times, the first 100 drag times, and the full  $10^3$ -drag time simulation duration, versus  $\cos \xi_0$ , for the 504 case-1 Davis-Greenstein simulations.

ping to be more severe for smaller grains, possibly resolving the contradiction. However, with the introduction of nuclear relaxation, Lazarian & Draine (1999b) concluded that all grains are likely thermally trapped. We conclude that thermal trapping is not prevalent for either  $a_{\text{eff}} = 0.2 \mu\text{m}$  or  $a_{\text{eff}} = 0.05 \mu\text{m}$ .

Jones & Spitzer (1967) noted that if grains contain superparamagnetic inclusions, then the D-G alignment time-scale could be dramatically reduced. If only the relatively large grains contain superparamagnetic inclusions, then D-G alignment could be consistent with the Kim & Martin (1995) results (Mathis 1986). We will examine D-G alignment for the case of grains with superparamagnetic inclusions in future work. From the results in this work, we conclude that D-G alignment without superparamagnetic inclusions is unlikely to account for alignment of the relatively large grains responsible for the observed optical and infrared starlight polarization, in the diffuse ISM. However, it is the long alignment time, rather than any thermal trapping effect, that renders it unlikely.

Hoang et al. (2014) argued that small grains must be aligned to some extent in order to explain the observed ultraviolet starlight polarization and proposed that the observations could be used to

estimate the interstellar magnetic field strength. They examined D-G alignment of small grains, assuming that these grains are thermally trapped. Our results show that suprathreshold spin-up may be important for the small grains, potentially yielding higher degrees of alignment. However, this conclusion is sensitive to the details of the H<sub>2</sub>-formation model. We adopted  $t'_{\text{life}} = 1$  in our simulation with  $a_{\text{eff}} = 0.05 \mu\text{m}$  (case 7), but smaller values are plausible and would yield a smaller degree of alignment. Furthermore, Weingartner & Draine (2001) argued that a model in which the grain surface is saturated in chemisorption sites, as considered in section 6.4.1 above, is plausible. In this case, any systematic torque would be negligible, precluding suprathreshold spin-up. We will more carefully examine D-G alignment of small grains in future work.

### 13 CONCLUSIONS

In this study, we first extended the analysis of Barnett relaxation in Kolasi & Weingartner (2017) beyond the low-frequency limit, enabling an approximate treatment of both Barnett and nuclear relaxation in thermally rotating grains. Since no first-principles theory of Barnett or nuclear relaxation has been developed to date, there is considerable uncertainty in the quantitative expressions for the drift and diffusion coefficients. We followed Kolasi & Weingartner (2017) in assuming that the diffusion coefficient goes to zero at  $q = r_3$ . We also neglected any deviation of the functional forms for the drift and diffusion coefficients from their low-frequency forms.

Next, we developed theoretical expressions for the mean torque and diffusion coefficients for several external processes, including collisions of gas-phase particles with the grain, thermal evaporation from the grain surface, and the formation of H<sub>2</sub> molecules, followed by their ejection from the grain surface. These apply for the special case of a spheroidal grain with a non-uniform mass density (with the center of mass at the center of the spheroid and the principal axis of greatest moment of inertia lying along the spheroid symmetry axis). We adopted several simplifications in the analysis of H<sub>2</sub>-formation. The translational kinetic energy of the ejected molecules is taken to be constant. In the case of special formation sites on the grain surface, the ejection rate is taken to be equal at all of the sites and the molecules depart along a single direction at each site.

From large simulation suites, in which the Langenvin equations for both internal and external processes are integrated, we reach the following conclusions. First, the mean duration of up-steps (when the systematic torque acts so as to spin the grain up) exceeds the mean duration of down-steps. Second, thermal trapping is not prevalent during crossovers. Third, the Davis-Greenstein mechanism, with suprathreshold spin-up, can drive grains into alignment in the cold neutral medium, without significant impediment from thermal trapping. However, it does not appear to be a viable explanation of grain alignment in the diffuse ISM, at least for the relatively large grains that are responsible for optical and infrared starlight polarization, since the alignment time-scale is long. The D-G mechanism could, however, potentially yield some small-grain alignment, with observable consequences for ultraviolet starlight polarization. Future work will examine this possibility in greater detail.

Currently, the consensus view is that radiative torques dominate in the alignment of relatively large grains; see Lazarian (2007) and Andersson et al. (2015) for reviews. This view has resulted, in part, from the conclusion of Lazarian & Draine (1999b) that grains subjected only to torques that are fixed relative the grain body are

thermally trapped. We conclude that, even without thermal trapping, D-G alignment does not effectively align large grains.

Detailed models have found that, in the radiative-torque alignment scenario, grains can pass through crossovers and can reach aligned states characterized by either suprathreshold or thermal rotation (Weingartner & Draine 2003; Hoang & Lazarian 2009). Thus, the main result of this paper, that the mean duration of up-steps exceeds the mean duration of down steps, could have significant implications for radiative-torque alignment as well as for D-G alignment. In future work, we will adapt the computational and theoretical tools developed here to a study of radiative-torque alignment. We will also consider grains with superparamagnetic inclusions.

Finally, Purcell (1979) focused on grain alignment, but also noted that the tensile stress within a suprathresholdly rotating grain could possibly disrupt the grain, depending on its structure. Recently, Hoang and collaborators (e.g. Hoang et al. 2019; Hoang 2019, 2020; Lazarian & Hoang 2020) have developed this idea in detail, with a focus on radiative torques. The grain equilibrium rotational rates for the model of H<sub>2</sub>-formation torques adopted here are shown in Fig. 5 and equation (162). Comparing with Fig. 13 in Lazarian & Hoang (2020) and Figs. 12–15 in Draine & Weingartner (1997), these are comparable to results from previous studies of H<sub>2</sub>-formation torques and can exceed the rotational rates arising from radiative torques, for conditions typical of the CNM. Thus, our conclusion that thermal trapping is not prevalent could have significant implications for the rotational disruption of grains, especially in environments where radiative torques are weak. See Section 9.4 in Lazarian & Hoang (2020) for more details. The uncertainties associated with the H<sub>2</sub>-formation model, noted at the end of Section 12 above, will need to be resolved in order to clarify the importance of the resulting torques to grain disruption.

### ACKNOWLEDGEMENTS

We are grateful to Bruce Draine and the anonymous referee for helpful comments on the manuscript.

### DATA AVAILABILITY

The data underlying this article will be shared on reasonable request to the corresponding author.

### REFERENCES

- Andersson B. G., Lazarian A., Vaillancourt J. E., 2015, *ARA&A*, **53**, 501  
 Davis Jr. L., Greenstein J. L., 1951, *ApJ*, **114**, 206  
 Draine B. T., Weingartner J. C., 1997, *ApJ*, **480**, 633  
 Hoang T., 2019, *ApJ*, **876**, 13  
 Hoang T., 2020, *Galaxies*, **8**, 52  
 Hoang T., Lazarian A., 2009, *ApJ*, **695**, 1457  
 Hoang T., Lazarian A., Martin P. G., 2014, *ApJ*, **790**, 6  
 Hoang T., Tram L. N., Lee H., Ahn S.-H., 2019, *Nature Astronomy*, **3**, 766  
 Jones R. V., Spitzer Lyman J., 1967, *ApJ*, **147**, 943  
 Kim S.-H., Martin P. G., 1995, *ApJ*, **444**, 293  
 Kolasi E., Weingartner J. C., 2017, *MNRAS*, **471**, 1222  
 Lazarian A., 2007, *J. Quant. Spectrosc. Radiative Transfer*, **106**, 225  
 Lazarian A., Draine B. T., 1997, *ApJ*, **487**, 248  
 Lazarian A., Draine B. T., 1999a, *ApJ*, **516**, L37  
 Lazarian A., Draine B. T., 1999b, *ApJ*, **520**, L67  
 Lazarian A., Hoang T., 2020, Alignment and rotational disruption of dust ([arXiv:2010.15301](https://arxiv.org/abs/2010.15301))

- Lee H. M., Draine B. T., 1985, *ApJ*, 290, 211  
Mathis J. S., 1986, *ApJ*, 308, 281  
Peters T., et al., 2017, *MNRAS*, 467, 4322  
Press W. H., Teukolsky S. A., Vetterling W. T., Flannery B. P., 1992, Numerical Recipes in FORTRAN; The Art of Scientific Computing, 2nd edn. Cambridge University Press, New York, NY, USA  
Purcell E. M., 1979, *ApJ*, 231, 404  
Purcell E. M., Spitzer Jr. L., 1971, *ApJ*, 167, 31  
Roberge W. G., Lazarian A., 1999, *MNRAS*, 305, 615  
Roberge W. G., Degraff T. A., Flaherty J. E., 1993, *ApJ*, 418, 287  
Spitzer Jr. L., McGlynn T. A., 1979, *ApJ*, 231, 417  
Weingartner J. C., 2009, *ApJ*, 690, 875  
Weingartner J. C., Draine B. T., 2001, *ApJ*, 553, 581  
Weingartner J. C., Draine B. T., 2003, *ApJ*, 589, 289

This paper has been typeset from a  $\text{\TeX/L\AA\TeX}$  file prepared by the author.